Experimental observation of moduli dispersion and attenuation at seismic frequencies in saturated tight rock: effect of microstructure and fluid viscosity

Yan-Xiao He ⓘ,[1] Sanyi Yuan,[1] Genyang Tang ⓘ,[1] Chao Sun,[2] Yuzhao Feng,[1] Junliang Yuan,[3] Zhanxun Feng,[4] Chunhui Dong,[1] Peidong Shi[5] and Shangxu Wang[1]

[1]*State Key Laboratory of Petroleum Resources and Engineering, College of Carbon Neutral Energy, College of Carbon Neutrality Future Technology, College of Geophysics, CNPC Key Laboratory of Geophysical Exploration, Sinopec Oil Reservoir Integrated Geophysical Research Centre, China University of Petroleum (Beijing), Beijing 102249, China. E-mails: eeyhe123@163.com (Yan-Xiao He); wangsx@cup.edu.cn (Shangxu Wang)*
[2]*China University of Mining and Technology, School of Resources and Geosciences, Xuzhou, Jiangsu Province 221116, China*
[3]*CNOOC Research Institute Ltd, Beijing 100028, China*
[4]*Geology Research Institute, CNPC Greatwall Drilling Company, Panjin, Liaoning Province 124010, China*
[5]*School of Earth and Environmental Sciences, Cardiff University, Cardiff, Wales CF10 3AT, UK*

SUMMARY

The frequency-dependent elastic properties of fully saturated rocks are notably influenced by fluid pressure diffusion at the microscopic scale. Our experimental evaluation, utilizing forced oscillation and ultrasonic transmission methods under varying effective pressures ($P_{\text{eff}} = [1 - 20]$ MPa) and temperatures ($T = [3℃, \ 10℃, \ 23℃]$), provides critical insights into how rock microheterogeneity and pore fluid viscosity affect elastic dispersion and attenuation at frequencies of $f = [1 - 300, \ 10^6]$ Hz. We employed a sandstone rock sample with 8.2 per cent porosity and conducted measurements using three different fluids: N_2, brine and glycerine. In its dry state, our chosen rock exhibits frequency independent elastic moduli at measured effective pressures due to the absence of fluid flow, resulting in negligible deviations in local measurements at different locations. However, this uniform response changes markedly when the rock is saturated with fluids. Gassmann's predictions agree with the measured undrained elastic moduli. Under fluid-saturated conditions, rock's elastic moduli increase with frequency, revealing significant differences depending on measurement positions. This variation suggests that differentiation in elastic properties is amplified during wet measurements, particularly at seismic frequencies. Our modelling indicates that the dominant mechanism is squirt flow, arising from microscopic compressibility heterogeneities within the rock frame and saturating fluid. As the viscosity of the saturating fluid decreases with rising temperature, the magnitude of attenuation peaks diminishes, while their frequency spread widens. This behaviour aligns with predictions from the squirt flow model, which considers the microstructure and varied pore types within the rock. Consequently, the observed frequency dependence in elastic moduli is primarily attributed to fluid flow processes driven by microheterogeneity, which are highly sensitive to small variations in the rock's microstructures. In microstructurally complex regions, it is evident that assuming isotropic and homogeneous conditions for forced axial oscillation measurements can introduce errors. The inherent heterogeneity of the rock must be taken into account to accurately interpret the frequency dependence of elastic moduli. This is especially relevant for applications in geophysical hydrocarbon exploration and seismic monitoring of reservoir geomechanical integrity during CO_2 geo-sequestration.

Key words: Elasticity and anelasticity; Microstructure; Acoustic properties; Seismic attenuation.

1 INTRODUCTION

The accuracy of reservoir and geomechanical simulation strongly relies on the rock elastic stiffness utilized in the model. Owing to a scarcity of core samples, the dynamic elastic properties of crustal rocks are typically derived from seismic methods $(1 - 100\,\text{Hz})$ or sonic logging measurements ($\sim$kHz) measurements. Generally, fluid-saturated sedimentary rocks exhibit higher and frequency-dependent elastic properties compared to dry samples (e.g. see Spencer 1981; Cooper 2002; Batzle *et al.* 2006; Adelinet *et al.* 2010; Pimienta *et al.* 2015; He *et al.* 2024a). Ideally, seismic elastic dispersion and attenuation (Q^{-1}) estimated from field measurements could provide critical parameters such as porosity, permeability, fluid content and saturation in fluid-rock systems. These systems include unconventional hydrocarbon reservoirs, subsurface saline aquifers for CO_2 geosequestration, nuclear waste deposits, or even partially fluid–solid or solid–solid coexisted subsurface regions (e.g. see Tisato & Quintal 2013; Zhao *et al.* 2017). However, the relationship between seismic elastic moduli and these reservoir parameters is complex and not yet fully understood. Therefore, it is crucial to capture all the underlying physical processes that dominate seismic elastic properties and their related attenuation in microstructurally complex and variable rocks saturated with viscous fluids under natural subsurface conditions (e.g. Spencer 2013; Borgomano *et al.* 2019; He *et al.* 2022 and references therein).

Rock properties obtained from field and laboratory measurements are highly dependent on environmental conditions such as temperature, pressure and frequency, leading to ambiguous comparisons due to various known and unknown factors that contribute to the upscaling problem. It is important to consider the causality-bound dispersion and attenuation behaviours of rock properties, which arise from viscous-driven fluid flows at different scales in the rock's pore system and are frequency- and distance-dependent. These factors are crucial for developing field-relevant applications like improving the inversion of the rock and fluid properties using seismic data (e.g. Müller *et al.* 2010; Tisato & Quintal 2013). Controlled experimental investigations offer promise for achieving a deeper understanding of these interplay between fluid flow and microstructure and the underlying mechanisms. Additionally, due to intrinsic rock heterogeneities, dynamic elastic measurements at a certain scale and location (or representative elementary volume, REV) may not represent the same rock properties as those obtained using different techniques at varying frequencies (e.g. David *et al.* 2013; Yin *et al.* 2017; Sun *et al.* 2020). For instance, attenuation in hydrocarbon deposits measured from sonic logging is often higher than that observed from seismic measurements, which can be attributed to frequency dependence or microstratification effects.

The effects of frequency on the attenuation and dispersion of elastic moduli in fully fluid-saturated rocks, from seismic to ultrasonic $(10^5 - 10^6\,\text{Hz})$ frequencies, have been extensively documented for sandstones (e.g. David *et al.* 2013; Mikhaltsevitch *et al.* 2014; Tisato *et al.* 2015; Spencer & Shine 2016; Pimienta *et al.* 2017; Han *et al.* 2018; Chapman *et al.* 2019; Sahoo *et al.* 2019), carbonate rocks (e.g. see Batzle *et al.* 2006; Adam *et al.* 2009; Adelinet *et al.* 2010; Mikhaltsevitch *et al.* 2016a; Borgomano *et al.* 2019; He *et al.* 2023) and shales (e.g. Piane *et al.* 2014; Mikhaltsevitch *et al.* 2021; Rorheim *et al.* 2022). Despite these observations, the impacts of rock microheterogeneity at the REV scale and the influence of fluid viscosity variations with temperature on elastic dispersion and attenuation of tight rocks have been barely explored (e.g. Subramaniyan *et al.* 2015; Borgomano *et al.* 2017). Most sedimentary rocks are inherently heterogeneous, with complex microstructures and a variety of pore types, yet few studies have specifically addressed how these factors contribute to the observed frequency-dependent phenomena. As pointed out by Szewczyk *et al.* (2018) and discussed in more detail elsewhere, the frequency-dependent phenomenon of stress sensitivity in elastic waves may be attributed to stress-related micromechanical processes. An increase in effective pressure leads to several changes: the closure of microcracks with small aspect ratio, the stiffening of grain contacts and a decline in effective porosity, resulting in increased rock stiffness and elastic moduli (e.g. Shapiro 2003; de Paula *et al.* 2012; Glubokovskikh *et al.* 2016; Duan *et al.* 2018; Sun & Gurevich 2020). Understanding the interplay between rock microheterogeneity, fluid viscosity and frequency is crucial for improving our ability to interpret seismic data and better predict the mechanical behaviour of rocks in subsurface environments.

Regarding the wave-induced fluid flow (WIFF) effect, it has been demonstrated that the induced fluid pressure diffusion occurring across various spatial regions can be broadly categorized into microscopic, mesoscopic and macroscopic scales, as addressed in analytical studies presented by Mavko & Jizba (1991), Chapman (2003), Pride *et al.* (2004), Gurevich *et al.* (2010), Müller *et al.* (2010), Deng & Morozov (2016), Gurevich & Carcione (2022), Alkhimenkov (2024), Alkhimenkov & Quintal (2024) and literatures therein. Several literatures have reported that frequency-dependent phenomena are important in rocks saturated with two fluid phases (e.g. Tisato & Quintal 2013; Chapman *et al.* 2016; Li *et al.* 2019; Wei *et al.* 2021), and attempted to verify the applicability of the Biot–Gassmann's relations (e.g. Borgomano *et al.* 2017; Sun *et al.* 2022), the wave-induced gas exsolution dissolution mechanism (e.g. Chapman *et al.* 2017), the dual-scale fluid flows (e.g. Borgomano *et al.* 2017; Sun *et al.* 2020; Zhao *et al.* 2021), the gas bubble resonance model (e.g. Sahoo *et al.* 2019) or the Zener rheological model (e.g. Pimienta *et al.* 2017; Borgomano *et al.* 2019). Accurate numerical solutions were introduced recently to help understand attenuation and velocity dispersion of seismic waves in poroelastic rocks (e.g. Carcione & Gurevich 2011; Quintal *et al.* 2016; Lissa *et al.* 2020; Alkhimenkov & Quintal 2022; Zhang *et al.* 2023 and literatures therein), as well as delineating the accuracy and the range of validity of the analytical model. Recent laboratory measurements have also highlighted that local fluid flow, or squirt flow, is the primary mechanism for dispersion and attenuation in porous rocks (e.g. Subramaniyan *et al.* 2015; Yin *et al.* 2017; Borgomano *et al.* 2019). This mechanism arises due to the presence of grain-scale damage zones, broken grain contacts, or microcracks of various shapes and orientations. Foundational works by O'Connell & Budiansky (1977) and Mavko & Jizba (1991) describe this squirt-flow attenuation mechanism, which has traditionally been considered significant only at ultrasonic frequencies. However, recent studies suggest that squirt flow may also substantially impact seismic exploration and sonic frequencies. As pointed out in de Paula *et al.* (2012) and Rubino & Holliger (2013), among several other laboratory experiments, several key factors contribute to squirt flow dispersion near seismic frequencies, including viscous fluids, declined permeability, complex microstructures and heterogeneous pore types of rocks. Microscopic complexity, such as mineralogy, the heterogeneous distribution of compliant pore aspect ratios, crack density and variety of pore types, can significantly influence mesoscopic and even macroscopic elastic properties like Young's modulus and bulk and shear moduli. Despite their importance, these microscopic parameters or rock intrinsic heterogeneity are often challenging to access in field observations, making it

difficult to assess the impact of local dispersive phenomena on wave propagation at the REV scale.

To the authors' knowledge, few published studies report investigations on the induced differences between the total rock elastic properties derived from the mean values of all local measurements and the locally measured results at approximately the REV scale at different positions. This gap in research is critical, as it can lead to a better understanding of how intrinsic rock heterogeneity influences elastic properties and wave propagation. Notable exceptions include the works of Sun *et al.* (2020) and He *et al.* (2022), which have begun to explore these differences under the assumption of homogeneity and isotropy at the REV scale. Given the complexities and limitations in current research, more attention should be paid to the microscopic complexity of rock local measurements and their implications for mesoscopic and macroscopic elastic properties.

Understanding the complexity of microstructures inherent in tight sandstones and their impact on wave-induced fluid flow, which results in the attenuation and dispersion of dynamic moduli, remains a significant challenge. Distinguishing these effects from experimental measurements (both ultrasonic and low frequencies) or field observations (such as seismic and sonic logging) is particularly challenging due to the intricate nature of the rock fabric and fluid interactions. To investigate the influences of diverse rock microstructures and fluid viscosity (η) on dispersive and attenuative elastic properties, we conducted a series of laboratory experiments using the forced oscillation and ultrasonic pulse transmission (UPT) methods. These experiments spanned a frequency band of $f = [1 - 10^3, \ 10^6]$ Hz, were conducted under various effective pressures, and utilized different pore fluids in a particular tight sandstone known for its pronounced microheterogeneity. For the experiments, relatively large core plugs (~ 38 mm in diameter and ~ 70 mm in length) were used. This size allowed us to examine the influences of heterogeneities at the millimeter- and centimeter-scales. The sandstone sample was sequentially saturated with different fluids—nitrogen gas (N_2), glycerine, and brine—each maintained at a constant pore pressure $P_P = 1.2$ MPa. Following a concise description of the tested sandstone, the experimental apparatus, and the measurement protocol, we present the experimental results, emphasizing the sensitivity of Young's modulus (E), extensional attenuation (Q_E^{-1}), bulk modulus (K), and shear modulus (μ) to changes in frequency and fluid viscosity (η).

The collective results of the experiments indicate that elastic dispersion and attenuation in tight sandstone are significantly influenced by both the viscosity of the saturating fluid and the frequency of the applied stress. According to existing fluid-flow theories, local fluid movement within the microstructure, particularly around grain contacts and microcracks, plays a crucial role in governing the elastic properties of tight sandstones. These findings highlight the necessity of considering the microstructural complexity of rocks and the associated local fluid-flow mechanisms when interpreting seismic and sonic logging data.

2 SPECIMEN STUDIED AND EXPERIMENTAL METHODS

2.1 Specimen characterization and preparation

The sandstone sample TS4 examined in this study is originated from a deep well in Shahejie formation, situated at a depth of approximately 3850–3875 m in the Bohai Bay basin, China, and is

Table 1. Mineralogical composition and physical properties of the tight sandstone specimen determined by XRD analysis.

Sample diameter, d (mm)	38
Sample length, L (mm)	70
Sample's porosity, ϕ (per cent)	8.2
Sample's helium permeability, κ ($\times 10^{-15}$ m^2)	0.052
Bulk modulus of solid grains, K_g (GPa)	38
Density of solid grains, ρ (kg m^{-3})	2640
Quartz (per cent)	76.3
Feldspar (per cent)	7.6
Calcite (per cent)	5.5
Clay (per cent)	3.4
Error on measured low-frequency K and μ (per cent)	± 2.6

regarded as a typical tight hydrocarbon reservoir rock. The core plug, extracted nearly parallel to the bedding using a precision core drill, was cut into cylindrical specimen around 70 mm in length and 19 mm in radius for testing at China University of Petroleum (Beijing). The surface and both ends of the specimen were meticulously trimmed with a surface grinder to eliminate weakly cemented grains, thereby mitigating the impact of surface roughness on experimental measurements. X-ray diffraction (XRD) analysis reveals that the framework grains and cement of the core plug are primarily consist of quartz (~ 76.3 per cent), feldspar (~ 7.6 per cent), calcite (~ 5.5 per cent) and clay (~ 3.4 per cent), as detailed in Table 1. The rock specimen was selected for its visual homogeneity, and elastic properties of the solid materials, K_g and μ_g, were derived from the volumetric contribution of each mineral alongside their respective elastic properties, employing the Voigt–Reuss–Hill average. Scanning electron microscopy (SEM) photomicrographs, along with two thin-section microscopic images of the selected plug under reflected light microscope, are presented in Fig. 1, showcasing the rock's properties, fabric and microstructures related to cracks, as well as grain size distribution, pore types and connectivity. The sample contains some clasts and significant microporosity of approximately 1.5 μm, a characteristic frequently observed in tight sandstones. This tested sample appears to have experienced through substantial compaction, resulting in a homogenous and fine-grained texture. The uniform rock matrix contains grains smaller than 100 μm that are moderately well sorted (Figs 1e and f). Rock's microstructure reveals a reasonably cemented composition, with some intergranular porosity present.

Measurements conducted on a dry sample extracted from the same batch of material as the one tested here indicate a porosity range of 7.8 per cent $-$ 8.2 per cent using helium as the reference fluid under effective pressures between 1 and 30 MPa (Fig. 2b). To evaluate potential microstructural alterations and framework damage during the oscillation and pressure cycle experiments, porosity was determined by weighing the dry and fully water-saturated core plug post-experimentation, resulting in a value of 7.4 per cent $\pm$ 2.3 per cent. The core permeability κ spans five orders of magnitude, from approximately 7×10^{-6} m^2 in the glycerine-saturated measurement to 5×10^{-1} m^2 with helium as the reference fluid, exhibiting varying dependences on effective pressure P_{eff}. Furthermore, to reduce the impact of open-pore boundary effects and contact friction between the epoxy and strain gauges, the core specimen surface with an impermeable fluorinated ethylene–propylene film coated with a thin epoxy layer, as opposed a single thick epoxy layer (see He *et al.* 2024b).
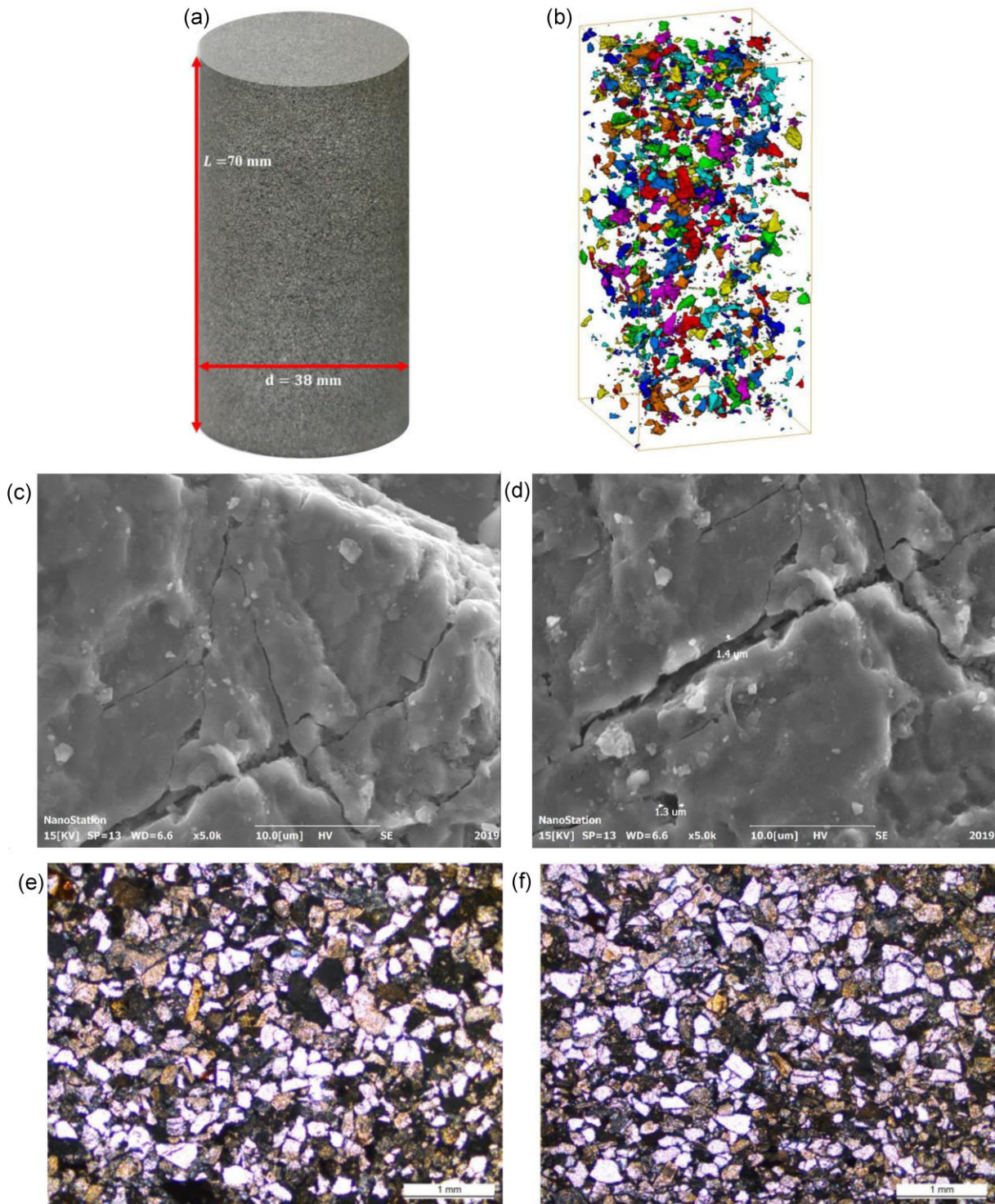
Figure 1. (a) Photograph of tested specimen TS4, (b) 3-D pore volume of the 3 mm diameter core, (c) and (d) field emission SEM images and (e) and (f) microscopic images of two thin sections of the tight sandstone at the same scale (1 mm).

2.2 Experimental system

In this study, the forced-oscillation based stress–strain (FOSS) technique was employed to characterize the dispersion (i.e. frequency-dependence) and attenuation of the elastic moduli of a saturated core sample (e.g. Spencer 1981; Batzle *et al.* 2006). Fig. 3 illustrates a schematic diagram of the experimental setup and sample stack with

attached strain gauges. The versatile experimental system facilitates measurements of both high-frequency (HF) ultrasonic *P*- and *S*-wave velocities along the sample axis using the ultrasonic pulse transmission technique, and low-frequency (LF) dynamic elastic parameters (Young's modulus *E* and its associated dissipation Q_E^{-1}, along with Poisson's ratio *ν*) over the $1 - 2000$ Hz range for tested
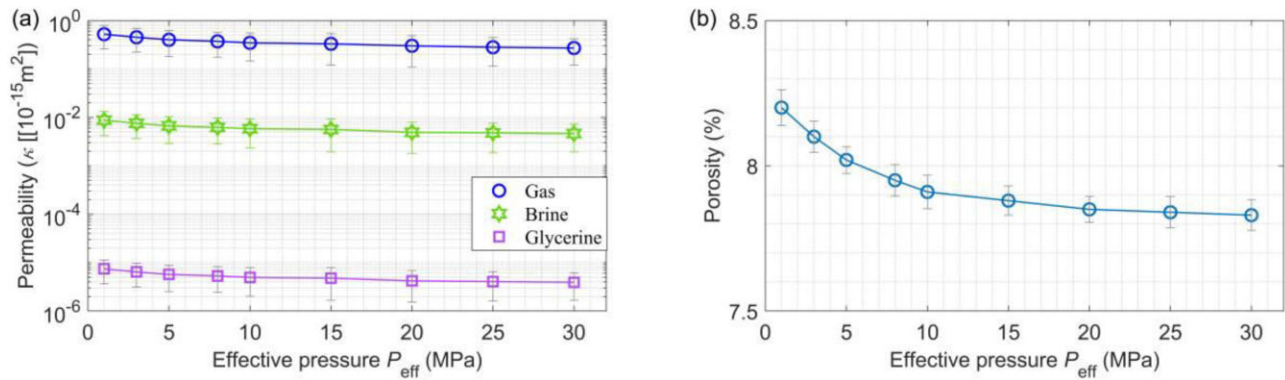
Figure 2. Measurements and error bars of the pressure dependence of (a) intrinsic permeabilities κ in the sandstone sample under dry, glycerine-, and brine-saturated conditions at $T = 23^{\circ}$C, and (b) porosity ϕ of the dry sample. Note the *in situ* viscosities of glycerine and brine are approximately $\eta_{gly} = 1.22$ Pa·s and $\eta_{bri} = 1.05 \times 10^{-3}$ Pa·s, respectively.

specimens within a single experiment at different confining pressures ($P_C = [0 - 40]$ MPa), pore pressures ($P_P = [0 - 15]$ MPa) and temperatures ($T = [0^{\circ} - 60^{\circ}]$). Two pairs of semiconductor strain gauges measure strains in the axial direction, and two pairs measure strains in the radial direction. Two gauges in the axial deformation direction are bonded to the non-dispersive aluminum endplate. An electromechanical oscillator exerts a sinusoidal axial force amplified by a source signal amplifier. Two pairs of in-house built compressional and shear wave piezoelectric transducers (~ 1 MHz) embedded in the top and bottom aluminum endplates are crucial to HF and LF measurements, respectively. For more detailed descriptions of our novel laboratory facility, please see Yin *et al.* (2017) and He *et al.* (2024b).

The experimental apparatus used in our study is capable of performing measurements at strain magnitudes maintained approximately between 10^{-8} and 10^{-6} m m−1, ensuring the measurements are within the linear elastic regime of the rock specimen. This range is relevant for both LF applications in the field and HF theoretical analyses (see Rorheim *et al.* 2022). Small strains in both axial and radial directions are measured locally on the sample using bonded resistive displacement sensors, specifically strain gauges with a size of 1×5 mm^2. These sensors are capable of accurately capturing the expansion and contraction of the tested specimen (see Fig. 3c), helping in characterizing the elastic response of the specimen to stress. Specifically, the measuring region covered by the strain gauges is larger than the REV considered for the rock specimen. The REV is large enough to be approximately homogeneous but much smaller than the overall scale of the sample. By ensuring that the REV is appropriately sized, experimental measurements can be considered representative of the rock's bulk properties while still capturing the effects of microstructural heterogeneity. The phase angles between the applied axial stress and the resulting strain, as well as between the radial and axial strains, are recorded. This allows for the determination of the complex Young's modulus E^* and Poisson's ratio υ^*.

In addition, due to the small radial signal amplitudes relative to axial displacements, the measured Poisson's ratio υ and its associated attenuation Q_υ^{-1} exhibit more scattered features. Nevertheless, the Young's modulus E and its attenuation Q_E^{-1} measurements tend to follow steady trends. Correspondingly, for an elastic, isotropic, and homogeneous specimen, the Young's modulus and Poisson's ratio from axial stress oscillations can be calculated using the following relationships

$$E = \frac{\varepsilon_{alu}}{\varepsilon_{ax}} \cdot E_{alu} \text{ and } \upsilon = \frac{\varepsilon_{rad}}{\varepsilon_{ax}}, \tag{1}$$

here ε_{alu} and E_{alu} represent the mean axial strain and Young's modulus of the aluminum endcaps, respectively, and ε_{rad} and ε_{ax} represent the mean magnitudes of radial and axial strains, respectively. Then, we can obtain other elastic properties, such as the axial bulk modulus K and shear modulus μ, using the known complex moduli E and υ (e.g. see Spencer & Shine 2016; Chapman *et al.* 2019; Lozovyi & Bauer 2019)

$$K = \frac{E}{3(1 - 2\upsilon)} \text{ and } \mu = \frac{E}{2(1 + \upsilon)}. \tag{2}$$

Note that uncertainties in the measurements of E and υ, related to the average of the strains ($\Delta\varepsilon$), propagate through the formulations of other elastic properties. Nevertheless, the errors in the mean values decrease with an increasing number of strain gauges used, regardless of direction. For a completely isotropic and homogeneous material, there should be no significant deviation between different displacement sensors. In the case of poroelastic rocks, however, slight deviations between displacement sensors can occur due to the inherent heterogeneity of the rock microstructure. The resultant uncertainty can be evaluated by averaging the strain amplitudes (e.g. see Borgomano *et al.* 2019; He *et al.* 2024b). Furthermore, the associated attenuation of a complex elastic modulus $\tilde{H}$ (which can be bulk modulus, shear modulus or Young's modulus), usually quantified by the inverse quality factor Q_H^{-1}, measures the dissipated elastic energy during an oscillation cycle in viscoelasticity. This can be inferred from the phase shift between the applied stress (with phase φ_σ) and the resulting strain (with phase φ_ε) as follows

$$Q_H^{-1} = \frac{\text{Im}(\tilde{H})}{\text{Re}(\tilde{H})} = \frac{\text{Im}(\tilde{\sigma}/\tilde{\varepsilon})}{\text{Re}(\tilde{\sigma}/\tilde{\varepsilon})} = \tan(\varphi_\sigma - \varphi_\varepsilon). \tag{3}$$

Similarly, the calculation of attenuation Q_υ^{-1} for Poisson's ratio υ is given by

$$Q_H^{-1} = \tan(\varphi_{\varepsilon_{rad}} - \varphi_{\varepsilon_{ax}}), \tag{4}$$

where ($\varphi_{\varepsilon_{rad}} - \varphi_{\varepsilon_{ax}}$) represents the phase shift between the radial and axial strains. Note that the error in the phase measurements for our forced-oscillated apparatus is consistently around ± 0.002 rad.

2.3 Measurement protocol

Once specimen preparations are completed, the column assemblage can be placed inside a large pressure vessel, where independent
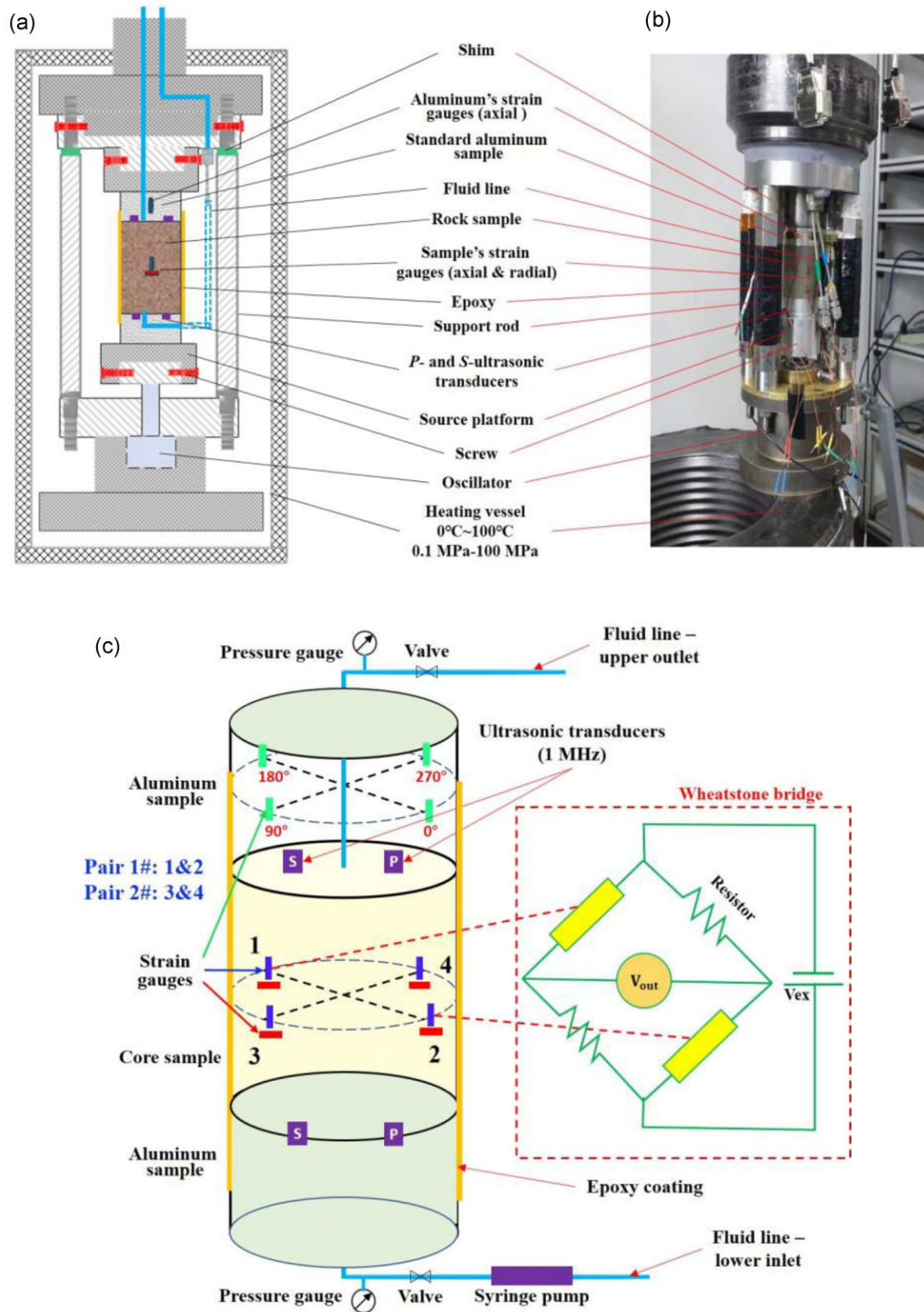
Figure 3. Schematic diagrams of (a) the experimental apparatus for the measurements of frequency-dependent elastic dispersion and attenuation, (b) a photograph of the sample stack and (c) the column assemblage, the key component of the low-frequency axial oscillation system, consisting of the test sample, two pairs of piezoelectric transducers, two aluminum endcaps, and a Wheatstone bridge for the weak strain signal output. The test sample is a cylinder with a length of $L \approx 7$ cm and a diameter of $d \approx 38$ mm, sealed from the nitrogen gas confining pressure with an epoxy coating. A vessel was designed for loading pressure and temperature. The mechanical unit (b) can be put into the vessel for mimicking *in situ* high-pressure, high-temperature measurements. A multislice piezoceramic actuator is applied as the stress load to induce dynamic axial-stress oscillations.

Table 2. Characteristics of pore fluids used in the experiments (see Sheng & Jian 1998).

Properties of pore fluids at ∼ 1 MPa	Nitrogen gas (at 23°C)	Glycerine (at 23°C)	Glycerine (at 10°C)	Glycerine (at 3°C)	Brine (at 23°C)
Bulk modulus (GPa)	$K_{NG} = 0.001\,42$	$K_G = 4.61$	$K_G = 4.84$	$K_G = 4.96$	$K_B = 2.25$
Density (kg m^{-3})	$\rho_{NG} = 11.62$	$\rho_G = 1260$	$\rho_G = 1275$	$\rho_G = 1286$	$\rho_B = 1015$
Viscosity ($\times 10^{-3}$ Pa·s)	$\eta_{NG} = 0.017$	$\eta_G = 1220$	$\eta_G = 4000$	$\eta_G = 7600$	$\eta_B = 1.05$

Table 3. Summary of performed experiments.

Pore fluid	Effective pressure (MPa) LF	HF	Temperature (°C)	Experimental procedure
Nitrogen gas	1 to 20	1 to 50	23°C	First test
			23°C	Second test 1
Glycerine	1 to 20	1 to 50	10°C	Second test 2
			3°C	Second test 3
Brine	1 to 20	1 to 50	23°C	Third test

controls exert confining pressure P_C (using compressed nitrogen gas as the medium) and pore pressure P_P on the test sample. Laboratory experiments conducted at seismic and ultrasonic frequencies using the FOSS and UPT techniques, respectively, can be divided into three cycles under N$_2$-, brine- and glycerine-saturated conditions for sample TS4 (refer to Tables 2 and 3). Measurements were initially conducted in the dry state, followed by glycerine-saturated conditions, and finally under brine-saturated conditions. Glycerine fully dissolves in water, losing its viscosity. Full brine saturation was achieved via flushing the core specimen four to five times its pore volume. Despite the significant temperature dependence of glycerine's intrinsic viscosity, its other properties, such as bulk density and bulk modulus, exhibit minimal variation, thus negligibly affecting elastic property measurements. Therefore, rather than simulating *in situ* subsurface conditions, which was impractical given the core specimen's depth, experiments were conducted at temperatures $T = [3^{\circ}C, 10^{\circ}C, 23^{\circ}C]$ to concentrate on fluid viscosity-driven mechanisms influencing the test specimen's mechanical properties. The reduction in temperature T increased fluid viscosity η, which was the sole variable aside from the effective pressure increment from 1 to 20 MPa. This approach facilitated the direct comparisons of mechanical response variations due to changes in fluid viscosity and rock microstructure deformations. The physical properties of the pore fluids are detailed in Table 2. During laboratory experiments, a pore pressure of $P_P = 1.2$ MPa was chosen, and a constant axial stress of $\sigma_{ax} \approx 0.4$ MPa was exerted to the test specimen to prevent stress-related non-parallelism of the column assembly and maintain improved signal quality for both LF and HF measurements, at effective pressures P_{eff} of [1, 5, 10, 15, 20] MPa and [1, 3, 5, 8, 10, 15, 20, 25, 30, 35, 40, 45, 50] MPa, respectively. Each experimental measurement lasted an average 3 to 4 d, with nearly 24 hr allocated for temperature adjustments and another 24–36 hr for achieving sufficient fluid and stress equilibrium within rock open pore systems.

Three perfectly homogeneous and isotropic specimens were used to assess the measurement accuracy of our versatile laboratory apparatus. Dynamic elastic measurements of Young's modulus E and Poisson's ratio υ for non-porous titanium and aluminium materials are depicted in Figs 4(a) and (b), as functions of confining pressure P_C at specific frequencies $f = [1, 5, 20, 200]$ Hz.

Dispersive characteristics of the lucite are demonstrated through Young's modulus E and attenuation Q_E^{-1} measurements in Figs 4(c) and (d). The experimental results show reasonably good agreement with those reported in existing literature (e.g. Batzle *et al.* 2006; Huang *et al.* 2015; Pimienta *et al.* 2015), suggesting that observable discrepancies may be attributed to difference in specimen material and the varying conditions of each laboratory experiment. Additionally, the frequency-dependent Young's modulus measurements E were well-fitted with the Cole–Cole relation (Cole & Cole 1941), and the associated extensional attenuation curve, described by the typical Kramers–Kronig relationship (e.g. Landau & Lifshitz 1969; O'Donnel *et al.* 1981; Christensen 1982; Lienert & Manghnai 1990; Mavko *et al.* 2009; Mikhaltsevitch *et al.* 2016b), aligns well with the measured Q_E^{-1} across a wide frequency range. In fact, our laboratory measurements of the selected sample are casual, indicating that the dispersion and attenuation in elastic moduli may reflect the intrinsic nature of the tested material.

3 EXPERIMENTAL DISPERSION AND ATTENUATION RESULTS

3.1 Pressure dependence of the ultrasonic measurements

The pressure P_{eff} and pore fluid dependences for high-frequency *P*- and *S*-wave ultrasonic velocity (V_P and V_S) measurements, as well as the derived bulk modulus K_{HF} and shear modulus μ_{HF}, are illustrated in Fig. 5 for the tight specimen TS4, including their respective error bars. Measured V_P and K_{HF} from low-compressibility fluids of brine- and glycerine-saturated sandstones (at $T = 23^{\circ}$ C), which are substantially higher than those for nitrogen gas filled (or dry) rock at any given pressure, exhibit similar behaviours. Notably, V_P and K_{HF} are higher in the specimen saturated with more viscous fluid. The ultrasonic velocity measurement system is highly accurate in recording arrival times, and the relative uncertainties on V_P, V_S, K_{HF} and μ_{HF} measurements, which could arise from potential misalignment of the ultrasonic transducers with the end surface, were estimated to be approximately $\Delta V_P / V_P = 1.5$ per cent,
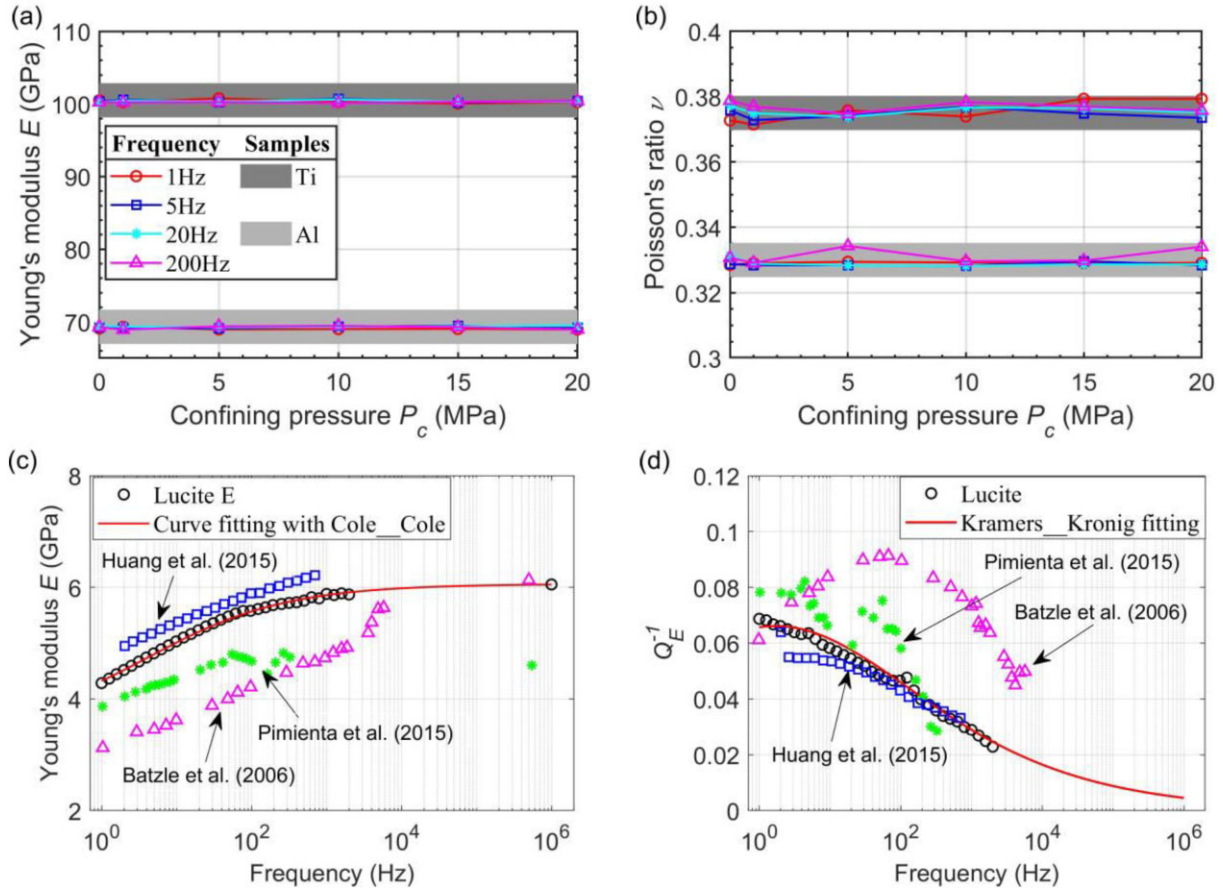
Figure 4. Measured pressure and frequency dependence of the elastic properties for the three reference samples of titanium, aluminium, and lucite from axial-stress oscillations with the apparatus. The Young's modulus E (a) and Poisson's ratio ν (b) of two standard samples at four different oscillation frequencies of $f = [1, 5, 20, 200]$ Hz are directly measured at confining pressures up to 20 MPa. The calibration results of Young's modulus E (c) and the corresponding extensional attenuation $1/Q_E$ (d) for the lucite sample as a function of frequency at a confining pressure of 2 MPa are illustrated, along with literature data from Batzle *et al.* (2006), Huang *et al.*(2015), and Pimienta *et al.* (2015). Parametric fits are applied to the experimental measurements and subsequently used to calculate E and $1/Q_E$ according to the Cole-Cole and Kramers–Kronig theories, respectively.

$\Delta V_S/V_S = 1.8$ per cent, $\Delta K_{HF}/K_{HF} = 1.82$ per cent   and $\Delta \mu_{HF}/\mu_{HF} = 2.6$ per cent.

The strong pressure sensitivities observed in elastic measurements confirm that the numerous naturally occurring microcracks in core plug TS4 progressively close during the pressurization cycle. This behaviour has been well-documented in previously published literatures on tight sandstone specimens and other kinds of rocks with similar microstructures (e.g. see David *et al.* 2013; Pimienta *et al.* 2015; Yin *et al.* 2017, and references therein). As observed, the *P*-wave ultrasonic velocity exhibits larger amplitudes and less pressure sensitivity with increasing bulk modulus of the pore fluid. Conversely, the *S*-wave velocity shows higher magnitudes at low pressures only. Beyond an effective pressure of $P_{eff} \sim 40$ MPa, under brine and glycerine saturation conditions, the V_P and K_{HF} results appear to stabilize and become constant with further increases in effective pressure. At an intermediate pressure of $P_{eff} \approx 12$ MPa for this specific core sample, there is an intersection point where the *S*-wave velocities from the dry and fluid-saturated specimens converge. Beyond this pressure, the *S*-wave velocities in brine and glycerine saturation are lower than those in the dry condition. This intersection point corresponds to the pressure at which the rock's acoustic signatures are significantly influenced by the presence of non-closable pores and cracks.

3.2 Frequency and pressure dependent measurements under dry condition

In this section, the frequency dependence of Young's modulus E_{LF} and Poisson's ratio ν_{LF}, along with their related attenuation ($Q_{E_{LF}}^{-1}$, $Q_{\nu_{LF}}^{-1}$), as well as the inferred bulk modulus K_{LF} and shear modulus μ_{LF} assuming isotropy, have been investigated for five effective pressures P_{eff} ranging from 1 to 20 MPa on the nitrogen gas-saturated specimen (see Fig. 6). During the experiments, the pore pressure was maintained at $P_P = 1.2$ MPa, and the confining pressure P_C was gradually increased between oscillation sequences. Dry ultrasonic measurements are also provided for comparison. System uncertainties in E_{LF}, ν_{LF}, K_{LF} and μ_{LF} of the dry rock, as indicated by the error bars, may be related to potential sources such as non-parallel alignment of strain gauges with respect to the specimen axis, slight misalignment of the device causing non-uniform distribution of stress and strain, and the high sensitivity of strain sensors to temperature and pressure variations. The low-frequency measurements from three successive experiments showed the following absolute uncertainties: $\Delta E_{LF} = \pm 0.45$ GPa, $\Delta \nu_{LF} = \pm 0.0035$, $\Delta K_{LF} = \pm 0.5$ GPa, and $\Delta \mu_{LF} = \pm 0.4$ GPa. The corresponding relative uncertainties were approximately $\Delta E_{LF}/E_{LF} = 2.5$ per cent, $\Delta \nu_{LF}/\nu_{LF} = 3.0$ per cent, $\Delta K_{LF}/K_{LF} = 4.5$ per cent and $\Delta \mu_{LF}/\mu_{LF} = 4.2$ per cent.
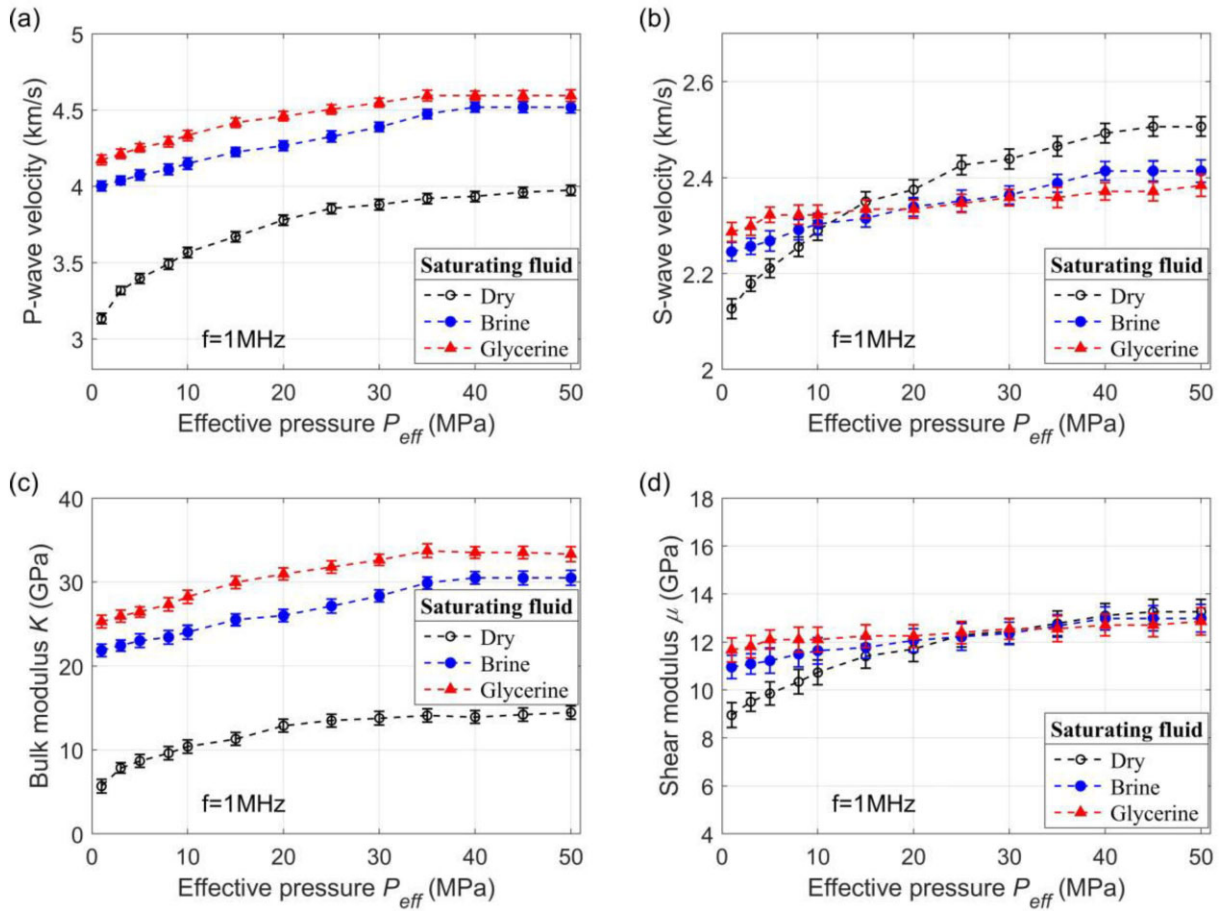
Figure 5. Experimental measurements for the porous specimen TS4 under nitrogen gas (dry), brine and glycerine saturation conditions at effective pressure P_{eff} up to 50 MPa with a maintained pore pressure at $P_P = 1.2$ MPa, under temperature $T = 23^\circ$ C. Graphs (a) and (b) show *P*- and *S*-wave velocities at an ultrasonic frequency of 1 MHz, and (c) and (d) display high-frequency bulk and shear moduli derived from elastic wave ultrasonic velocity measurements.

The specimen TS4 shows no measurable variation in elastic properties with frequency, correlated with attenuation; nevertheless, a significant effect of pressure is observed. It is also noteworthy that the measured low-frequency elastic properties (E_{LF}, υ_{LF}, K_{LF} and μ_{LF}) and the corresponding ultrasonic measurements exhibit similar values and follow the same pressure dependence. This indicates the absence of scattering effects from wave propagation or inertial effects in Biot's theory, which operate at frequencies much higher than those examined here (e.g. Sarout 2012). This variation feature is expected for assumed homogeneous isotropic materials when microcracks are gradually closed with increasing pressure P_{eff}. Furthermore, the dry specimen shows negligible LF attenuation, Q_E^{-1} and Q_v^{-1}, across the entire frequency range for the measuring pressures. The pressure dependence of dry ultrasonic elastic properties (moduli and velocities, in Fig. 5), which are non-dispersive, enables us to obtain heterogeneous distributions of the aspect ratio α of compliant pores and the cumulative crack density Γ of the stressed specimen TS4. This can be achieved using methods described in de Paula *et al.* (2012) and Duan *et al.* (2018).

At pressures of $P_{eff} = [5, 15]$ MPa, the dry moduli dispersion and attenuation measurements, as well as the inferred bulk and shear moduli, resulting from two pairs of strain gauges (gauges 1 & 2, and gauges 3 & 4 in Fig. 3c) for the tight core TS4 are presented in Fig. 7. While the differences in experimental results between

both pairs were found to be negligible over the frequency range studied, the elastic moduli of E_{LF}, υ_{LF}, K_{LF} and μ_{LF} from Pair 1# (circle symbols ○) are slightly larger than those from Pair 2# (cross symbols ×), with the magnitudes of relative difference less than 5 per cent. The aforementioned possible sources of experimental uncertainty can be greatly minimized through painstaking sample preparations. The higher the number of strain gauges, the lower the uncertainty becomes. Nevertheless, the locally measured dynamic strains on a cracked-porous specimen, which shows heterogeneous variations (e.g. internal variations of lamination) on a scale larger or comparable to the size of strain gauge used, are potentially the most obvious source of experimental inaccuracies. This is because all crustal rocks are inhomogeneous and/or anisotropic to a certain extent. This effect, highly depends on the quality of the local strain measurements, can be quantified by measurements with standard materials for which their elastic properties are known.

For the homogeneous isotropic materials, aluminium and lucite, the elastic properties measured and inferred (E_{LF}, υ_{LF}, K_{LF} and μ_{LF}) are reported as a function of frequency $f = [1 - 1000]$ Hz under low-Terzaghi effective pressure of $P_{eff} = 5$ MPa at room temperature (see Fig. 8). Similar to the porous specimen TS4, the results from both uncracked specimens exhibit negligible dependence on local strain measurements. The elastic properties from Pair 1# (circle marks ○) are consistent with those from Pair 2# (cross marks ×)

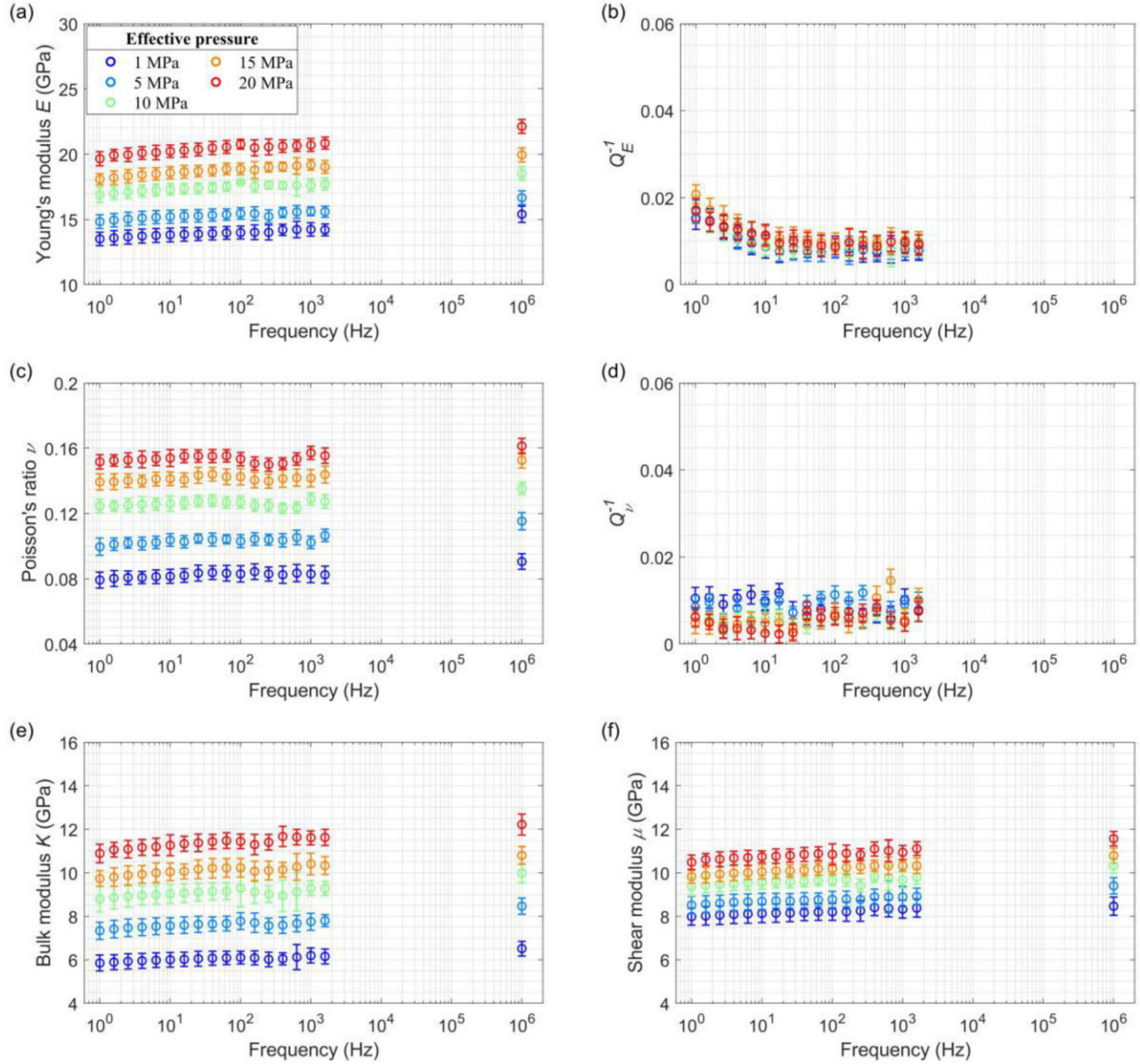**Figure 6.** Laboratory measurements for the frequency dependence of Young's modulus E (a) and Poisson's ratio ν (c), as well as the corresponding attenuation $1/Q_E$ (b) and $1/Q_\nu$ (d), and the derived bulk modulus K (e) and shear μ modulus (f) for the tight sandstone saturated with nitrogen gas as functions of effective pressure P_{eff} with a maintained pore pressure at $P_P = 1.2$ MPa, under temperature $T = 23^\circ$ C. The core sample was investigated at room temperature under isotropic loading with atmospheric pore pressure. Each open circle symbol represents the mean measurement of three experiments, with their corresponding error bars illustrated. Dry elastic moduli show errors of around ± 0.45 GPa for (a), ± 0.0035 for (c), ± 0.5 GPa for (e) and ± 0.4 GPa for (f). (b) and (d) have an error of ± 0.004 and ± 0.003, respectively.

across the tested frequency range. These sensitivity results confirm that the experimental apparatus allows for reliable measurement of the frequency dependence of elastic moduli using the forced oscillation method at the measured pressure.

3.3 Frequency and pressure dependence of elastic properties in fluid-saturated specimen

To explore the viscosity effects of the saturating fluid on rock elastic moduli measurements, two fluids with different intrinsic viscosities are chosen to saturate a homogeneous rock sample. The characteristic frequency at which dispersion and attenuation are

maximum varies as κ/η. The sample was maintained in an experimentally undrained boundary condition by closing the fluid pipelines during the axial stress oscillations and keeping fluid mass in the system (i.e. sample + dead volume). This setup allowed for the direct measurement of the dispersion and attenuation effects of the fluid-saturated specimen, particularly related to the squirt flow phenomenon. The elastic properties of low-permeability sandstone were investigated under full saturation with glycerine (high viscosity) and brine (low viscosity), respectively. The frequency dependence of Young's modulus E_{LF}, attenuation Q_E^{-1}, and the inferred bulk modulus K_{LF} and shear modulus μ_{LF} from two pairs of strain measurements at two effective pressures ($P_{eff} = 5$ and 15 MPa are reported in Fig. 9 for the brine-saturated specimen, and
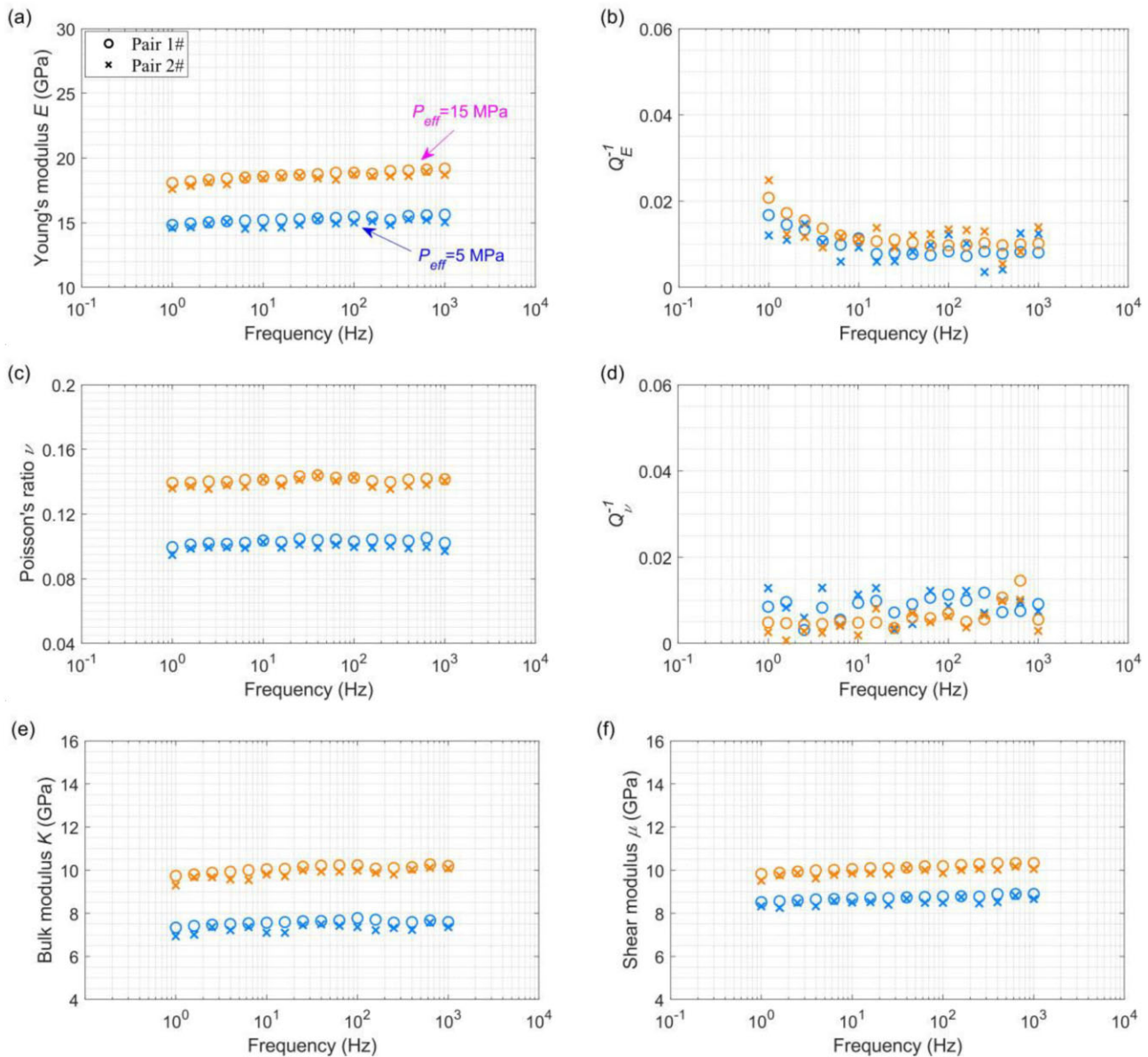
Figure 7. The measured frequency dependence of Young's modulus E is shown in graph (a) and Poisson's ratio ν in graph (c), with the corresponding attenuation $1/Q_E$ and $1/Q_\nu$ displayed in graphs (b) and (d), respectively, for a nitrogen gas-saturated sandstone sample at two effective pressures of 5 and 15 MPa at a pore pressure $P_P = 1.2$ MPa at $T = 23\,^\circ$C. Graphs (e) and (f) present the bulk modulus K and shear modulus μ, derived from the data in graphs (a) and (c). Additionally, circle marks (○) represent measurements from Pair 1#, while cross marks (×) are from Pair 2#.

in Fig. 10 for the glycerine-saturated specimen at temperatures of $T = [23\,^\circ$C, $10\,^\circ$C, $3\,^\circ$C].

For all fluid-saturated situations, Young's modulus, bulk modulus and shear modulus exhibit an increasing tendency with the increase of frequency. However, different dispersion characteristics are observed for brine and glycerine saturation. In the case of brine saturation, Young's modulus E_{LF} at an effective pressure of $P_{eff} = 5$ MPa increases slightly but remains in the range of approximately 19.5–22.5 GPa for frequencies below 600 Hz (Fig. 9a). Ultrasonic measurements of Young's modulus are significantly larger compared to the axial oscillation results. This suggests that the fluid pressure does not have sufficient time to be evenly distributed by the propagating ultrasonic waves. For the glycerine-saturated specimen, Young's modulus E_{LF} at $T = 23\,^\circ$C exhibits a gradual

increase from 22.5 GPa up to 31.5 GPa over the frequency band of experimentation (i.e. $f = [1 - 300; 10^6]$ Hz), and Young's modulus at $T = 3\,^\circ$C shows the largest magnitude, increasing from 27 GPa up to 35 GPa. For this low-permeability sandstone, the experimental results of E_{LF}, ν_{LF} and K_{LF} under glycerine saturation, which are clearly larger compared to the brine-saturated case, are slightly shifted to lower frequencies. These findings underscore the complex interplay between fluid viscosity, frequency, and temperature in influencing the elastic properties of rocks.

For all performed experiments, the effective pressure P_{eff} strongly affects the frequency dependence of Young's attenuation Q_E^{-1}, and a peak in frequency-dependent Young's attenuation is observed for two different P_{eff} values (see Figs 9b, 10b, f and j). As the frequency increases, Q_E^{-1} for $P_{eff} = [5, 15]$ MPa increases and shows large
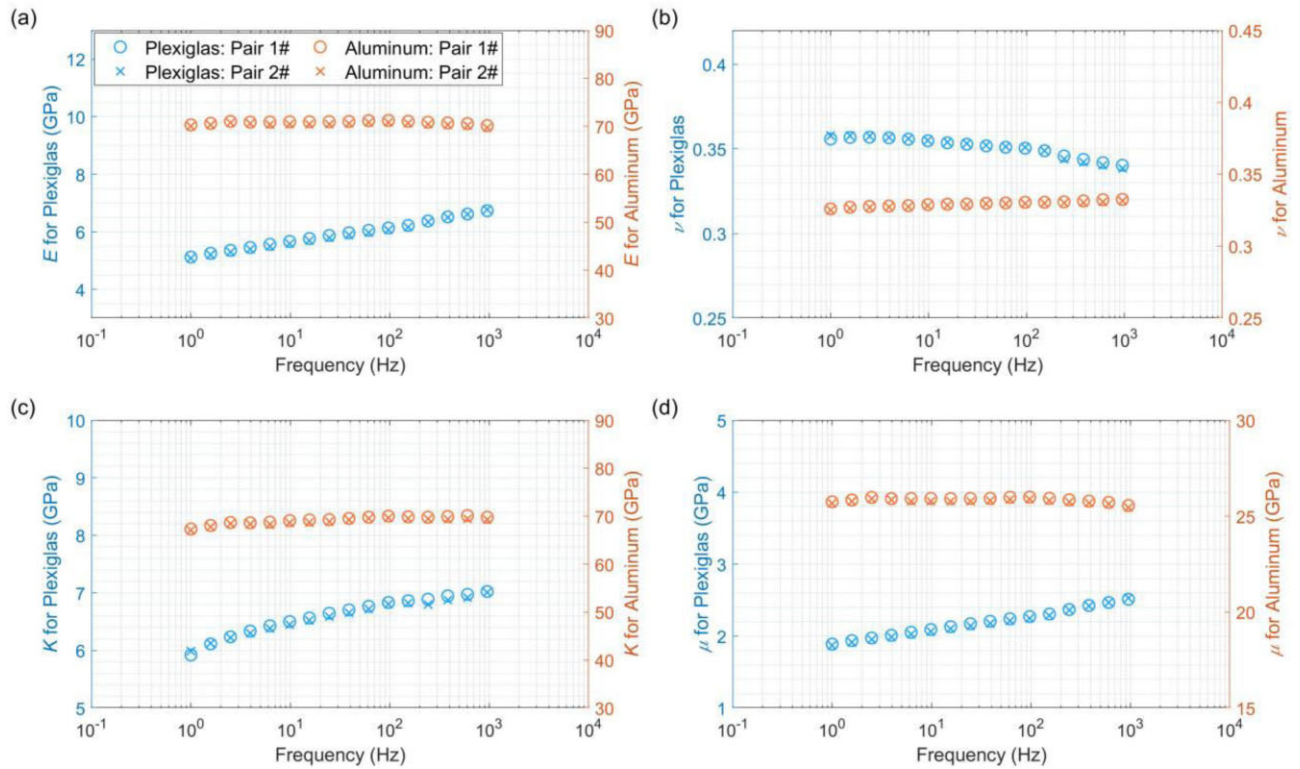
Figure 8. The measured Young's modulus E is shown in graph (a) and Poisson's ratio ν in graph (b). The inferred bulk modulus K is displayed in graph (c) and shear moduli μ in graph (d), all derived from low-frequency axial oscillations for the reference samples of aluminium and Plexiglas at $P_{\text{eff}} = 5$ MPa. Additionally, circle marks (o) represent measurements from Pair 1#, while cross marks ($\times$) from Pair 2#.

bell-shaped variations. It is worth noting that the E_{LF} measurements seem to show only one strong dispersion, which correlates with high-attenuation peaks. Although the peaks in Q_E^{-1} reduce substantially as effective pressure increases from $P_{\text{eff}} = 5$ to 15 MPa (pressure dependence), it seems that the Q_E^{-1} peak of the brine-saturated sample is smaller compared to the glycerine case. Similar to the elastic property results, the critical frequency corresponding to the Q_E^{-1} peak of the brine-saturated specimen shifts towards higher frequencies, compared to that of the glycerine-saturated specimen. For brine full saturation at $P_{\text{eff}} = 5$ MPa, Q_E^{-1} exhibits a maximum peak of approximately 0.07 at a frequency around $f_{\text{cb}-5} = 150$ Hz. For glycerine saturation, maximum peaks in Q_E^{-1} are approximately 0.085, 0.1 and 0.105 at $T = 23$, 10, and 3° C, respectively, at critical frequencies around $f_{\text{cg}-5} = 20$ Hz, $f_{\text{cg}-5} = 15$ Hz, and $f_{\text{cg}-5} = 12$ Hz. As effective pressure increases, the amount of fluid flow is consistently reduced due to the gradual closure of microcracks. To verify the consistency of measured results for the specimen under brine and glycerine saturation, the Kramers–Kronig (K–K) relations were used to examine the causality between E and Q_E^{-1} measurements. The good agreement between the obtained Young's modulus curves and the results of the K–K relations (Figs 9a, 10a, e and f) suggests that the experimental measurements are causal and possess a common physical mechanism involving the frequency dependence of E_{LF}. This agreement confirms the reliability and physical consistency of the measurements in the investigated wet specimen.

At two effective pressures, the obtained E_{LF}, Q_E^{-1}, K_{LF} and μ_{LF} from the brine- or glycerine-filled sample exhibit more pronounced discrepancies between two pairs of strain measurements compared to those in the dry (nitrogen gas) condition. This observation

underscores the importance of pore fluid in influencing the overall elastic stiffness of the specimen. In other words, the filled fluid, accessing the macropores through micropores or cracks, significantly affects the microheterogeneity of the rock. This interaction leads to local strain alterations on a scale larger than the size of strain sensors used, resulting in amplified differences in experimental measurements from two pairs of strain gauges in the fluid-saturated rock. At low frequencies ($f = [1 - 300]$ Hz), discrepancies in E_{LF} estimated at $P_{\text{eff}} = 15$ MPa are clearly smaller than those at $P_{\text{eff}} = 5$ MPa. This is consistent with the closure of microcrack as effective pressure increases. However, for the glycerine-saturated specimen at $T = 3°$ C, the associated magnitude of discrepancies shows a very different variation (Fig. 10f). It exhibits an increasing trend at $P_{\text{eff}} = 5$ MPa as frequency increases but a decreasing trend at $P_{\text{eff}} = 15$ MPa.

The selected sandstone sample exhibits observable local differences in microscopic pore structure, allowing for potential correlations between microstructure and squirt flow-induced dispersion and attenuation under fluid-saturated conditions. These correlations provide valuable insights into the mechanical behaviour of fluid-saturated rocks. In the case of fully brine saturation, discrepancies in E_{LF} between pairs of strain measurements decrease with increasing frequency for $P_{\text{eff}} = [5, 15]$ MPa. This decrease appears to correspond to the characteristic fluid diffusion length occurring in heterogeneous pore types. At higher frequencies, fluid movement within the pore structure becomes more homogeneous, and fluid pressure appears to have a more uniform distribution, reducing local strain variations. The magnitudes of bulk modulus K_{LF} and attenuation Q_E^{-1} at Pair 1# are lower compared to those at Pair 2#. Conversely, the Young's modulus E_{LF} and shear modulus μ_{LF} at

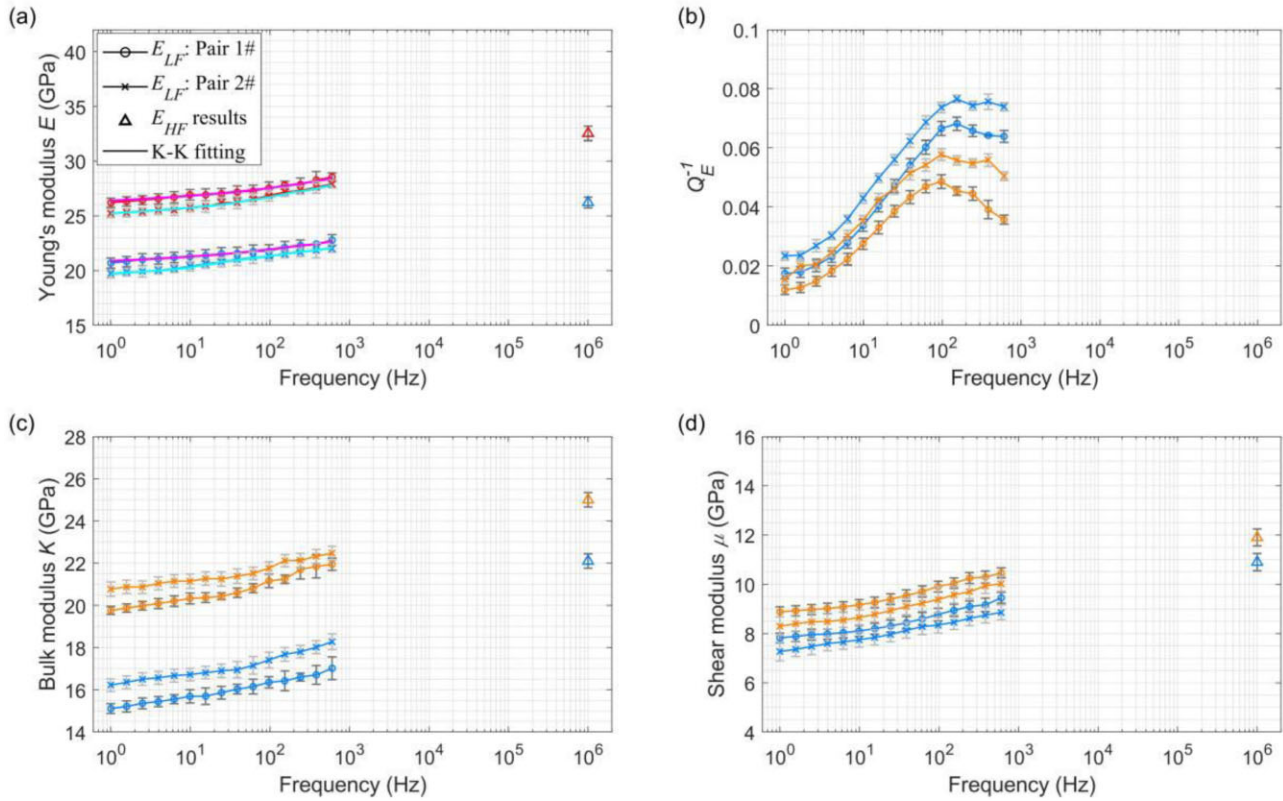**Figure 9.** Measurements at $P_{eff} = [5, 15]$ MPa under a maintained pore pressure $P_P = 1.2$ MPa, showing the frequency dependence of Young's modulus E (a) and Young's attenuation Q_E^{-1} (b) in the fully brine saturated sandstone sample at $T = 23°$ C. Graphs (c) and (d) show the derived bulk and shear modulus, respectively. Brine-saturated elastic moduli show errors of around ± 0.5 GPa for (a), ± 0.45 GPa for (c), and ± 0.54 GPa for (d). Measured Young's attenuation Q_E^{-1} (b) has an error of ± 0.003. Solid curves in graph (a) represent a parametric fit to the experimental measurements based on the Kramers–Kronig relationship. Note that each symbol of open circle (*o*) from Pair 1# and cross (×) from Pair 2# represents the mean measurement of three experiments, with corresponding error bars illustrated.

Pair 1# exhibit larger values than those at Pair 2#. For Q_E^{-1} measured from both pairs, the characteristic frequencies correlated with rock permeability κ seem to be the same, although these frequencies are shifted to much lower values due to the increase in fluid diffusion length. This shift is consistent with the expected microcrack closure as effective pressure P_{eff} increases from 5 MPa to 15 MPa (Fig. 9b). The variations in characteristic frequencies do not directly correlate with rock porosity or mineral properties, suggesting that other factors, such as pore structure and fluid distribution, play a more significant role.

Similar to the brine-saturated case, the characteristic frequencies for the two pairs of Young's attenuation (Q_E^{-1}) measurements were roughly identical under full glycerine saturation. This indicates that the characteristic frequencies are primarily governed by the rock's intrinsic properties, such as permeability and pore structure, rather than the type of saturating fluid. At two effective pressures, discrepancies between the two pairs of Q_E^{-1} measurements decrease as the temperature (T) drops from 23 to 3° C, which results in an increase in glycerine viscosity. With the increase in glycerine viscosity at lower temperatures, WIFF associated with the mobility of the high-viscosity fluid is suppressed, and the viscous friction-induced, frequency-dependent energy dissipation becomes more uniform within the pore spaces and microcracks. This equalization of energy dissipation results in more uniform attenuation across different regions of the specimen, reducing the discrepancies between the two pairs of Q_E^{-1} measurements.

At room temperature ($T = 23°$ C), the fluid viscosities of glycerine and brine used in the experiments are $\eta_{gly} = 1.22$ Pa·s and $\eta_{bri} = 1.05 \times 10^{-3}$ Pa·s, respectively. To account for both fluid viscosity and frequency effects within the framework of fluid flow theories associated with diffusion processes at different scales, a so-called 'apparent frequency' parameter f^a is introduced. This parameter normalizes the effects of fluid viscosity and frequency, allowing for a unified interpretation of the experimental results across different fluids and frequencies, as illustrated in Fig. 11. The concept of apparent frequency has been discussed in various studies and can be expressed as (e.g. see Pimienta *et al.* 2015; Spencer & Shine 2016; Borgomano *et al.* 2017)

$$f^a = f \times \frac{\eta_f}{\eta_0}, \tag{5}$$

where f represents the testing frequency of the applied stress, η_f denotes the considered fluid viscosity, and η_0 signifies the viscosity of brine. This approach scales the experimental frequencies according to the viscosity of the filling fluid, with brine as the reference. The *in situ* liquid viscosity of glycerine, which is used to determine the apparent frequency f^a, is derived from the measured intrinsic permeability of specimens filled with various fluids (Fig. 2). For testing frequencies $f < f_{Biot}$, the varying viscosity of the saturating fluid significantly extends the apparent frequency band of experimental measurements related to viscous fluid diffusion mechanisms by approximately three orders of magnitude, thereby characterizing the
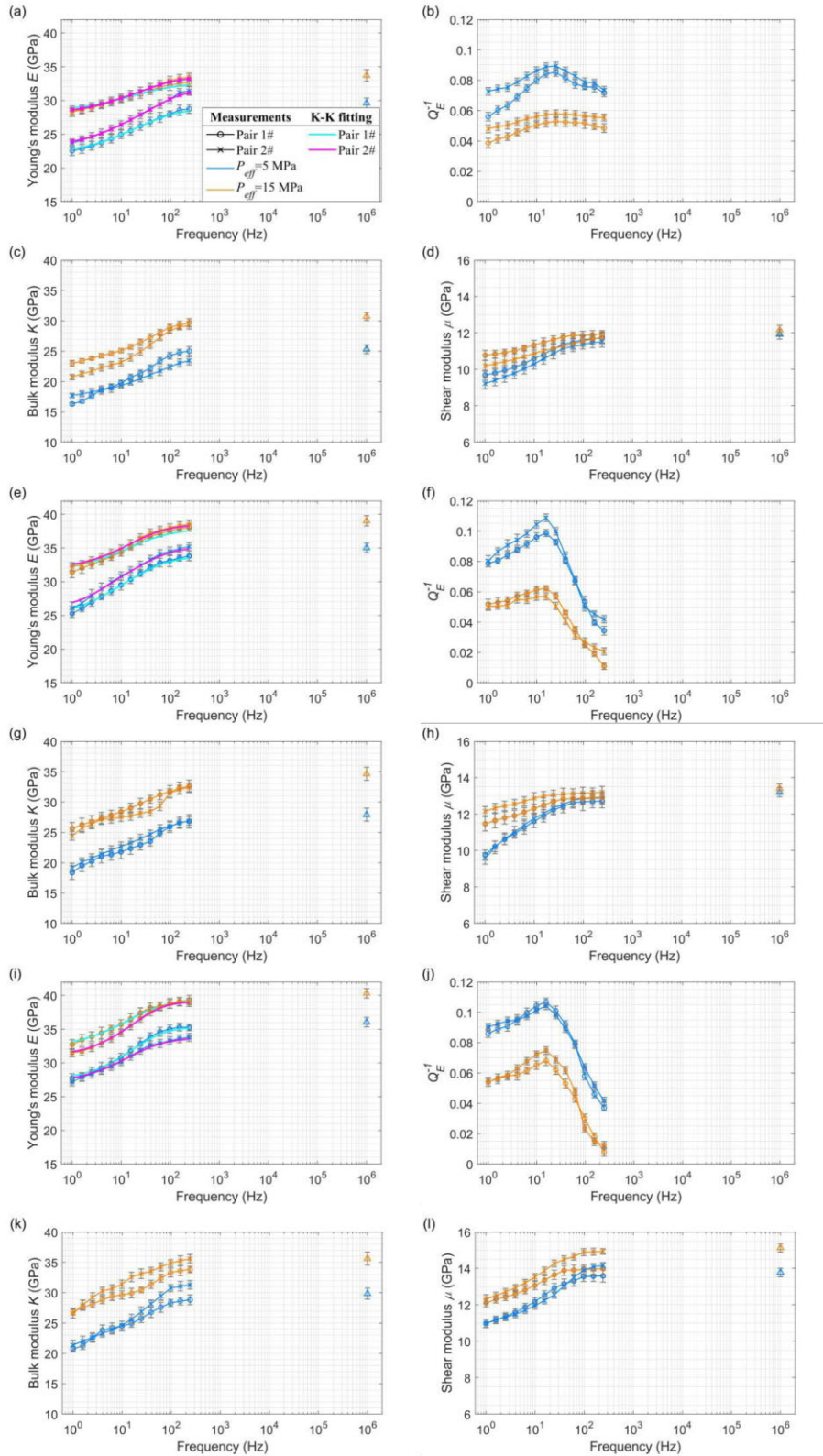
Figure 10. Measurements at $P_{eff} = [5, 15]$ MPa under a pore pressure $P_P = 1.2$ MPa, showing the frequency dependence of Young's modulus E, Young's attenuation Q_E^{-1}, and inferred elastic moduli in the fully glycerine-saturated sandstone sample at temperatures of (a)–(d) 23° C, (e)–(h) 10° C and (i)–(l) 3° C. Solid curves in graphs (a), (e), and (i) represent a parametric fit to the experimental measurements based on the Kramers–Kronig relationship. Note that each symbol of open circle (*o*) from Pair 1# and cross (×) from Pair 2# represents the mean measurement of three experiments, with corresponding error bars illustrated.
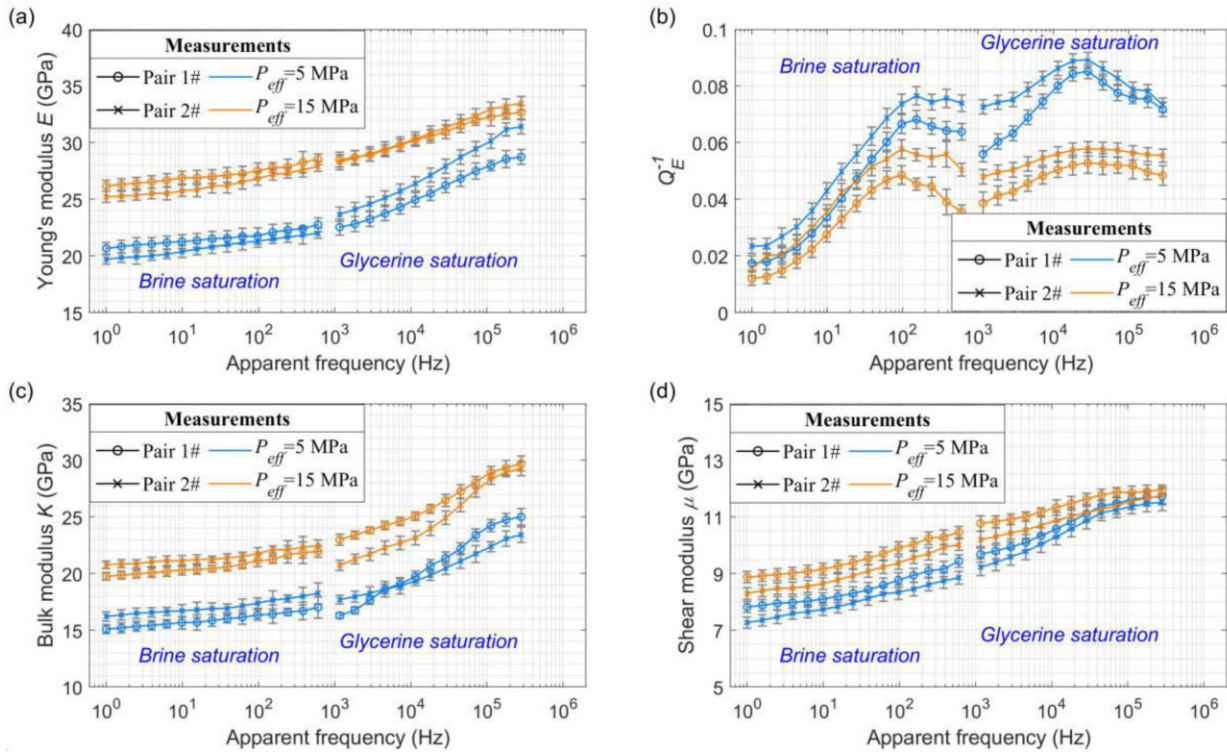
Figure 11. Results of (a) Young's modulus E, (b) the related attenuation Q_E^{-1}, and the inferred (c) bulk modulus K and (d) shear modulus μ in the fluid-saturated sample at 23° C at effective pressure $P_{\text{eff}} = [5, 15]$ MPa under a pore pressure $P_P = 1.2$ MPa. Apparent frequency f^a is scaled by the viscosity of the fluid, with brine as the reference fluid. For both pairs of measured results, two sets of measurements for brine (left) and glycerine (right) saturation conditions are plotted.

dispersion and attenuation effects of the saturated specimen over a wider frequency range. Biot's frequency, $f_{\text{Biot}} = \frac{\eta_f \phi}{2\pi D_f \kappa}$, where D_f is the fluid density, allows us to investigate the rock's elastic signatures under full brine-saturated conditions corresponding to well log frequencies (~ 10 kHz) in laboratory settings. Given the experimental apparatus's frequency band of $f = [1 - 600]$ Hz, the apparent frequency band under brine saturation is $f_{\text{bri}}^a = [1 - 600]$ Hz, and under glycerine saturation, it is $f_{\text{gly}}^a = [1.162 \times 10^3 - 2.9 \times 10^5]$ Hz at $T = 23°$ C.

The experimental results of E_{LF}, Q_E^{-1}, K_{LF} and μ_{LF} illustrated in Fig. 11 provide comprehensive insights into the elastic properties and attenuation behaviour of the sandstone samples under full brine and glycerine saturation at room temperature (23° C) for two different effective pressures (5 and 15 MPa), expressed in terms of apparent frequency f^a (e.g. Pimienta *et al.* 2017; Borgomano *et al.* 2019). The measured Young's modulus (Fig. 11a) and the inferred elastic moduli (Figs 11c and d) exhibit two notable dispersive transitions, evident under both saturation conditions at approximately 150 and 2×10^4 Hz, respectively. These transitions align with the peak values in Young's attenuation Q_E^{-1} (Fig. 11b). The results obtained around $f^a \approx 800$ Hz show a good agreement under both water and glycerine saturation for different pressures P_{eff}. Furthermore, the general evolutionary patterns of Young's modulus E_{LF} and attenuation Q_E^{-1}, as well as the elastic moduli K_{LF} and μ_{LF}, are consistent under both brine- and glycerine-saturated conditions. However, local strain measurements reveal two sets of elastic results that differ significantly with respect to f^a and P_{eff}. These variations can be primarily attributed to the intrinsic microheterogeneity and anisotropy of the specimens.

Additional potential sources of errors include the intrinsic bulk modulus of the fluids and the dynamic strain measurements by gauges (5 mm in length), which is larger compared to a REV average region. In the undrained regime of higher frequencies, the fluid mass remains constant, and pore pressure is isobaric within the REV.

4 INTERPRETATION OF EXPERIMENTAL RESULTS

4.1 Theoretical model for squirt flow dispersion and attenuation in fluid saturated rocks

In this study, different effects were observed for two pairs of local strain measurements in a low-permeability sandstone saturated with fluids of varying viscosities, such as nitrogen gas, brine and glycerine. As shown in Fig. 6, the sandstone specimen under dry conditions reveals no frequency dependence. Therefore, the measured dispersion and attenuation in the fluid-saturated sandstone are induced by the presence of pore fluids (Figs 9 and 10). Crustal rock generally contains pores and microcracks of various shapes, allowing saturating fluids to flow at different scales, from a compliant crack to a neighboring less compliant pores (e.g. Dvorkin *et al.* 1995; de Paula *et al.* 2012). In the undrained regime, the isobaric pressure status is maintained for pores within the REV but not for different REVs. The characteristic frequency corresponding to the drained/undrained transition can be expressed as follows (e.g. Mavko *et al.* 2009; Pimienta *et al.* 2017;

Borgomano *et al.* 2019)

$$f_{C1}^* = \frac{4K_d}{L^2}\frac{\kappa}{\eta}, \tag{6}$$

where K_d represents the drained bulk modulus and L is the sample's vertical length. Eq. 6 is valid for a laterally sealed core plug, accompanied by drained boundary conditions at the top and bottom. According to studies from O'Connell & Budiansky (1977), Mavko & Jizba (1991) or Gurevich *et al.* (2010), for example, the large dispersion and attenuation phenomenon, or squirt flow dispersion, relates to a transition separating the undrained and unrelaxed regimes. The corresponding characteristic frequency, which relies on core's macroscopic parameters of bulk modulus and fluid viscosity η, can be written as (e.g. Alkhimenkov & Quintal 2022; Alkhimenkov 2024; He *et al.* 2024a)

$$f_{C2}^* \approx \frac{K_m}{\eta}(\alpha_{sq})^3, \tag{7}$$

where K_m is the skeleton bulk modulus and α_{sq} is the so-called squirt flow aspect ratio controlling the characteristic frequency. This approach leverages the understanding that as effective pressure increases, compliant pores and microcracks close, leading to higher velocities and changes in the elastic properties of the rock. The sensitivity of pressure varies among different rock types due to variations in mineral composition, grain size, porosity and the distribution and connectivity of microcracks and pores. Also note that at higher frequencies, an additional attenuation peak may arise corresponding to the viscous shear relaxation mechanism. When the soft pores are contained with a Newtonian fluid of viscosity η, the characteristic frequency can be written as (e.g. Mavko 2013; Gurevich & Carcione 2022; Alkhimenkov 2024)

$$f_{C-shear}^* = \frac{2-\nu}{8(1-\nu)}\frac{\alpha G_{min}}{\eta}, \tag{8}$$

here, G_{min} and ν represent the mineral shear modulus and Poisson's ratio. However, the viscous shear relaxation in the fluid is negligible and beyond the scope in the current study. At $P_{eff} = 5$ MPa, $K_d = 8.3$ GPa, $L = 0.07$ m and $\kappa = 0.052 \times 10^{-15}$ m^2 are used for the dry sample. This results in a characteristic frequency $f_{C1}^* \approx 0.3$ Hz for the brine-saturated condition using eq. (6). The bulk skeleton bulk modulus estimated is $K_m = 38$ GPa. The squirt flow aspect ratio can be approximately by $\alpha_{sq} = h_{sq}/(2l_{sq}) \approx 1.6 \times 10^{-4}$, where h_{sq} and l_{sq} are thickness and length of squirt flow, respectively. Thus, the undrained/unrelaxed transition for squirt flow is expected to take place at $f_{C2}^* \approx 150$ Hz from eq. (7). The sample's mineral shear modulus is $G_{min} = 42$ GPa, and Poisson's ratio is $\nu = 0.1$. For the pore fluid of Newtonian, the characteristic frequency of shear relaxation in cracks may occur at $f_{C-shear}^* \approx 1.7$ GHz from eq. (8), which is much higher than the squirt characteristic frequency f_{C2}^*, and hence we only consider the squirt flow dispersion and ignore the viscous shear relaxation mechanism.

The study by de Paula *et al.* (2012) on dispersion and attenuation due to squirt flow between relatively compliant and relatively stiff pores demonstrated that it is reasonable to represent the total porosity ϕ can be represented as the sum of compliant (or soft) porosity ϕ_c, equant porosity ϕ_e, and moderately stiff or intermediate porosity ϕ_{ms}. Typically, ϕ_c is often 0.001 or less, ϕ_e has a characteristics aspect ratio close to 1, and ϕ_{ms} has aspect ratios between 10^{-3} and 2×10^{-1}. Therefore, the total porosity can be expressed as $\phi = \phi_c + \phi_e + \phi_{ms}$. Key parameters of the rock's pore microstructure can be derived based on the ultrasonic velocity measurements as a function of effective pressure, under the assumption that dry elastic properties are independent of frequency (non-dispersive). The aspect ratio α of microcracks, while difficult to measure directly with accuracy, can indeed be inferred from the exponential pressure dependence of dry elastic moduli (e.g. David & Zimmerman 2012; Duan *et al.* 2018). For a detailed description of the calculations used to determine the inhomogeneous distributions of aspect ratios $\alpha_c(P)$ and $\alpha_{ms}(P)$ for the compliant porosity $\phi_c(P)$ and intermediate porosity $\phi_{ms}(P)$, please refer to He *et al.* (2022). The pressure-dependent dry compressibility (open symbols), estimated from ultrasonic dry moduli measurements and the fitting (dashed curves), is shown in Fig. 12(a). Based on the pressure dependence of dry elastic properties (K_{dry}, G_{dry}), broad distributions for crack aspect ratios α_c^i at a given pressure P can be directly extracted using methods described by David & Zimmerman (2012)

$$\alpha_c^i(P) = \alpha_{c0}^i - \int_0^P \frac{4(1-\upsilon_B^2)}{3K_{sp}(1-2\upsilon_B)}dP, \tag{9}$$

where α_{c0}^i is aspect ratio of the ith un-stressed compliant pore, υ_B is Poisson's ratio of the solid skeleton, and K_{sp} is the bulk modulus of an isotropic background containing evenly distributed stiff pores. Accordingly, the compliant porosity distribution versus the aspect ratio α_c can be obtained using the following relationship

$$\phi_c^i(\alpha_c) = \frac{4}{3}\pi\alpha_c^i(P)\Gamma(\alpha_c), \tag{10}$$

where $\Gamma(\alpha_c)$ represents the cumulative crack density against aspect ratio α_c (see Fig. 12c) that can be directly obtained from elastic velocity measurements by applying a least-squares fitting method to match the experimental data with theoretical models. The pressure-dependent compliant porosity $\phi_c(P)$ is shown in Fig. 12(b), and the compliant porosity against aspect ratio α_c at five effective pressures is displayed in Fig. 12(d), where the main aspect ratio corresponds to the peak in the curves ϕ_c^i at each pressure.

Through the least-fitting of the stress-dependent dry rock elastic properties, key parameters for the intermediate pores ($\phi_{ms}(P)$, α_{ms}) can be derived by

$$K_{cp}(P) = K_{ep}[1 - \theta_{ms}\phi_{ms}(P)], \tag{11}$$

$$G_{cp}(P) = \mu_{ep}[1 - \theta_{ms}\phi_{ms}(P)]. \tag{12}$$

The calculated rock intermediate porosity $\phi_{ms}(P)$ as a function of P_{eff} is shown in Fig. 12(b). Similar to compliant pores, aspect ratio α_{ms} of the intermediate pores can be obtained by

$$\theta_{ms} = \frac{K_{ep}(3K_{ep} + 4G_{ep})}{\pi\alpha_{ms}G_{ep}(3K_{ep} + G_{ep})}. \tag{13}$$

Moreover, the dependence of bulk and shear moduli (K_{ep}, G_{ep}) of the dry rock skeleton on porosity can be described using (see Krief *et al.* 1990)

$$\frac{K_{sp}}{K_{ep}} = \frac{G_{sp}}{G_{ep}} = (1-\phi)^{3/(1-\phi)}, \tag{14}$$

here K_{sp} and G_{sp} represent dry frame elastic moduli of a hypothetical rock without open compliant pores.

Once the dry rock elastic properties, intermediate and compliant porosities, and their aspect ratios are extracted, the pressure- and frequency-dependent bulk and shear moduli of the fully saturated rock sample can be obtained using the modified Gassmann's equations

$$K_{sat}(P, \omega) = \left[\frac{1}{K_G} + \frac{\phi(1/K_f - 1/K_G)}{1 + \phi(1/K_f - 1/K_G)/(1/K_{mf}(P,\omega) - 1/K_G)}\right]^{-1}, \tag{15}$$
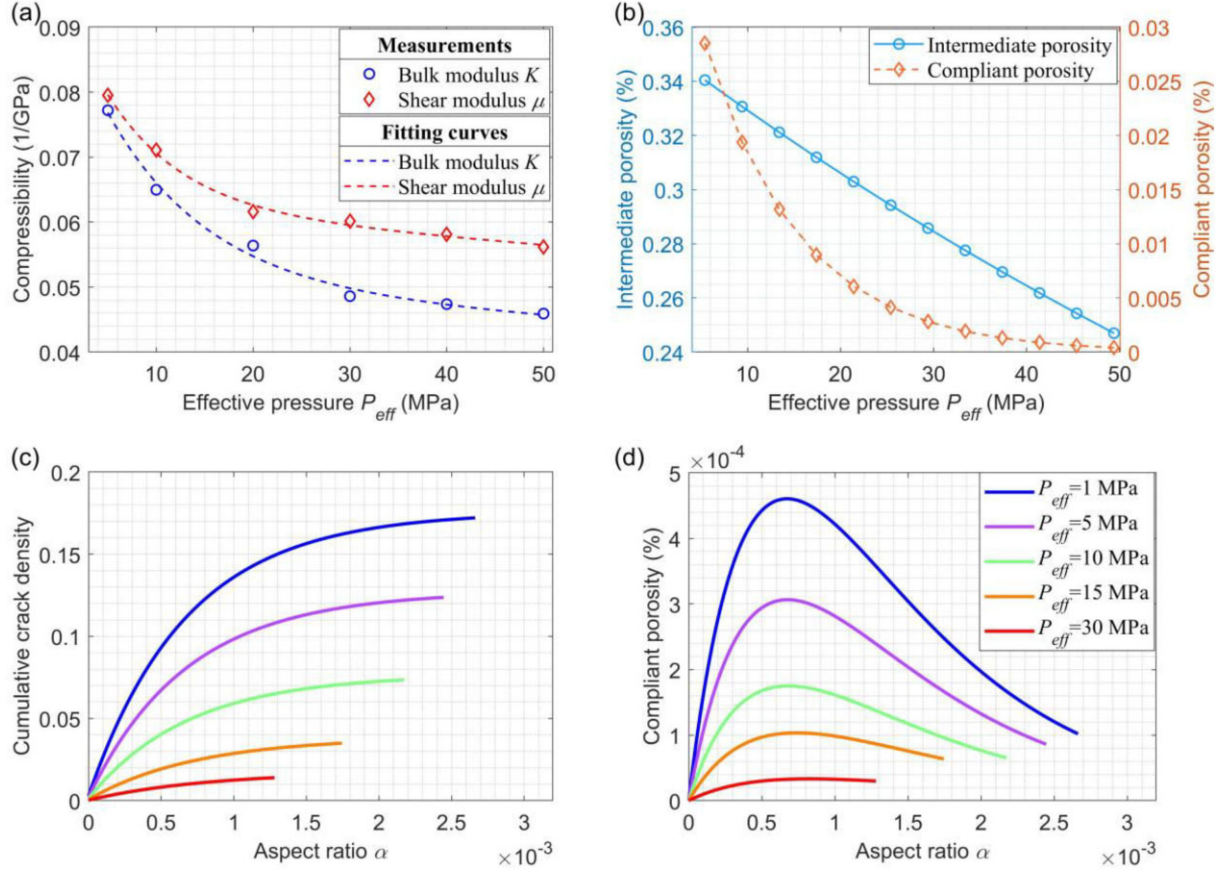
Figure 12. (a) Results of measured (symbols) and fitted (dashed lines) dry rock compressibility from bulk (circle) and shear moduli (diamond). (b) The estimated intermediate porosity ϕ_m (open circle) and compliant porosity ϕ_c (open diamond) as functions of P_{eff}. Note that the intermediate porosity declines approximately linearly up to 50 MPa. (c) The cumulative crack density and (d) the calculated crack porosity as functions of α at five effective pressures $P_{eff} = [1, 5, 10, 15, 20]$ MPa.

$$G_{sat}(P, \omega) = G_{mf}(P, \omega), \tag{16}$$

where K_f and K_g denote bulk modulus of the pore fluid and the solid mineral, respectively, and unrelaxed elastic moduli, $K_{mf}(P, \omega)$ and $G_{mf}(P, \omega)$, for the modified rock matrix can be written as (de Paula et al. 2012; He et al. 2022)

$$K_{mf}(P, \omega) = \left[\frac{1}{K_e} + \frac{1}{\left(\frac{1}{K_{cp}(P)} - \frac{1}{K_{ep}}\right)^{-1} + \frac{3i\omega\eta}{8\phi_{ms}(P)\alpha_m^2}} \right.$$
$$\left. + \frac{1}{\left(\frac{1}{K_{dry}(P)} - \frac{1}{K_{cp}(P)}\right)^{-1} + \frac{3i\omega\eta}{8\phi_c(P)\alpha_c^2}} \right]^{-1}, \tag{17}$$

$$G_{mf}(P, \omega) = \left[\frac{1}{G_{dry}(P)} - \frac{4}{15} \left[\frac{1}{K_{dry}(P)} - \frac{1}{K_{mf}(P, \omega)} \right] \right]^{-1}, \tag{18}$$

where $K_{cp}(P)$ represents the pressure-dependent unrelaxed dry bulk modulus of a hypothetical rock with all compliant porosity closed at relatively high pressures, and K_e represents the bulk modulus of a rock with the presence of only the equant pore, which is computed with self-consistent approximation effective medium model for spherical pores.

4.2 Sensitivity of elastic moduli to rock microheterogeneity and pore fluids

Comparisons between the experimental data and predicted results for Young's modulus E, attenuation Q_E^{-1}, bulk modulus K, and shear modulus μ for fully fluid-saturated sandstone at 23° C, based on two pairs of strain measurements at pressures $P_{eff} = [5, 15]$ MPa, are displayed as a function of apparent frequency f^a (see Fig. 13). The frequency-dependent elastic properties obtained using the squirt flow model in Gurevich et al. (2010), which incorporates a characteristic compliant pore aspect ratio (denoted as SF), generally align well with the experimental results under glycerine-saturated conditions. The squirt flow model that considers a triple pore structure and the effects of inhomogeneous aspect ratio distribution of compliant pores (denoted as SFTPS) also shows satisfactory agreement with the measured data. This model accounts for the variability in microscopic parameters such as aspect ratios and porosities of compliant and intermediate pores, reflecting the high sensitivity of microscopic squirt flow to changes in characteristic crack aspect ratios. At frequencies low enough (below Biot's frequency), both theoretical models converge to their undrained limits in Biot–Gassmann relations (Gassmann 1951; Biot 1962):

$$K_{sat}^{lf}(P) = \left[\frac{1}{K_G} + \frac{\phi(1/K_f - 1/K_G)}{1 + \phi(1/K_f - 1/K_G)/(1/K_{dry}(P) - 1/K_G)} \right]^{-1}$$
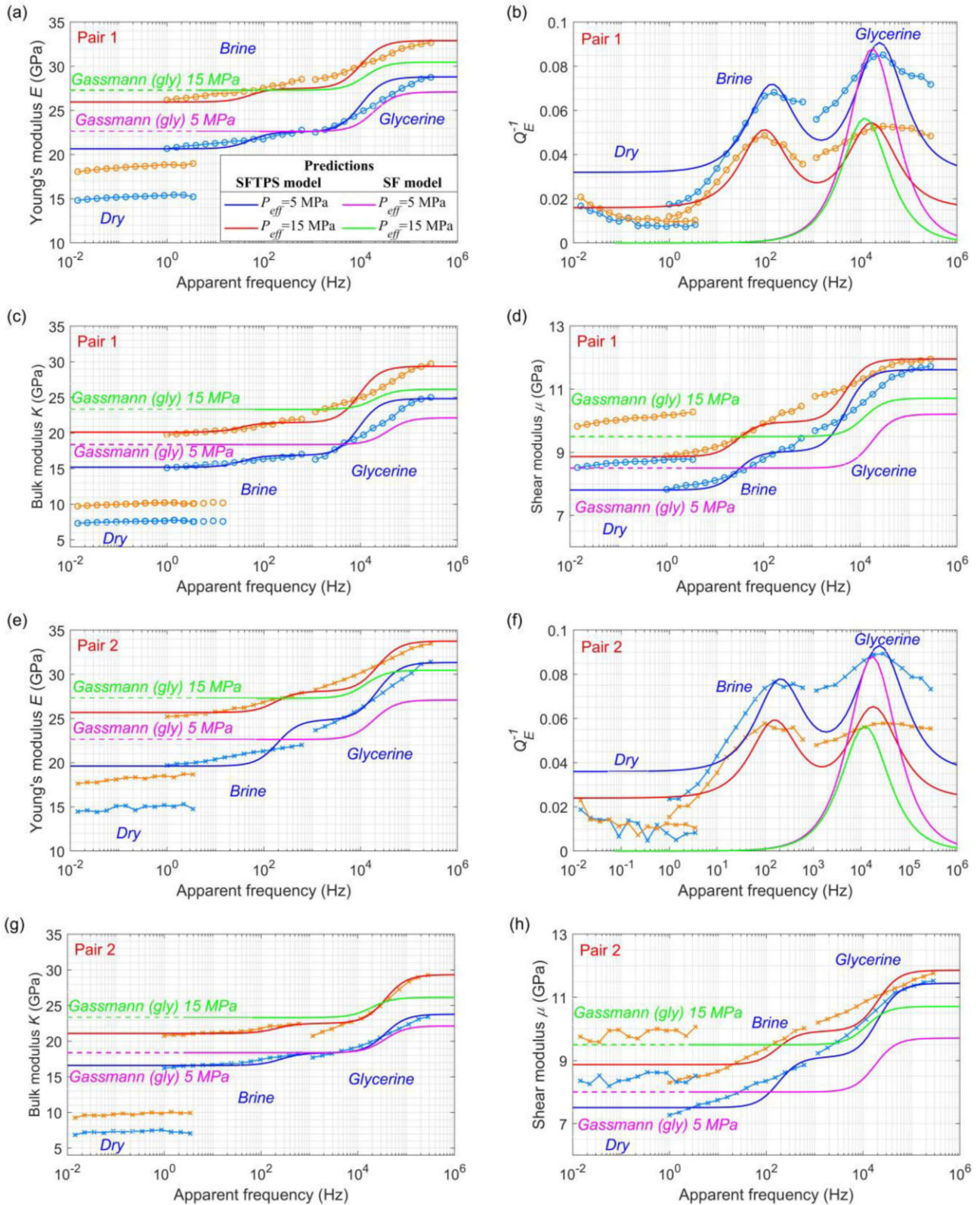$$\text{and } G_{sat}^{lf}(P) = G_{dry}(P). \tag{19}$$

Figure 13. Comparisons between laboratory measurements and predictions of Young's modulus E, Young's attenuation Q_E^{-1}, bulk modulus K and shear modulus μ as functions of apparent frequency f^a at effective pressures $P_{eff} = [5, 15]$ MPa. The measured results are shown for Pair 1# (graphs a-d, empty circle) and Pair 2# (e-h, cross) for samples saturated with brine and glycerine at $T = 23°$ C. In all cases, pink (5 MPa) and green (15 MPa) curves represent predictions from the Biot–Gassmann theory (horizontal dashed lines) and the SF model by Gurevich *et al.* (2010) with a characteristic aspect ratio of compliant pores (solid lines) under glycerine-saturated conditions. The solid blue (5 MPa) and red (15 MPa) curves are predictions from the SFTPS model of triple pore structure with an inhomogeneous aspect ratio distribution (see Fig. 12).
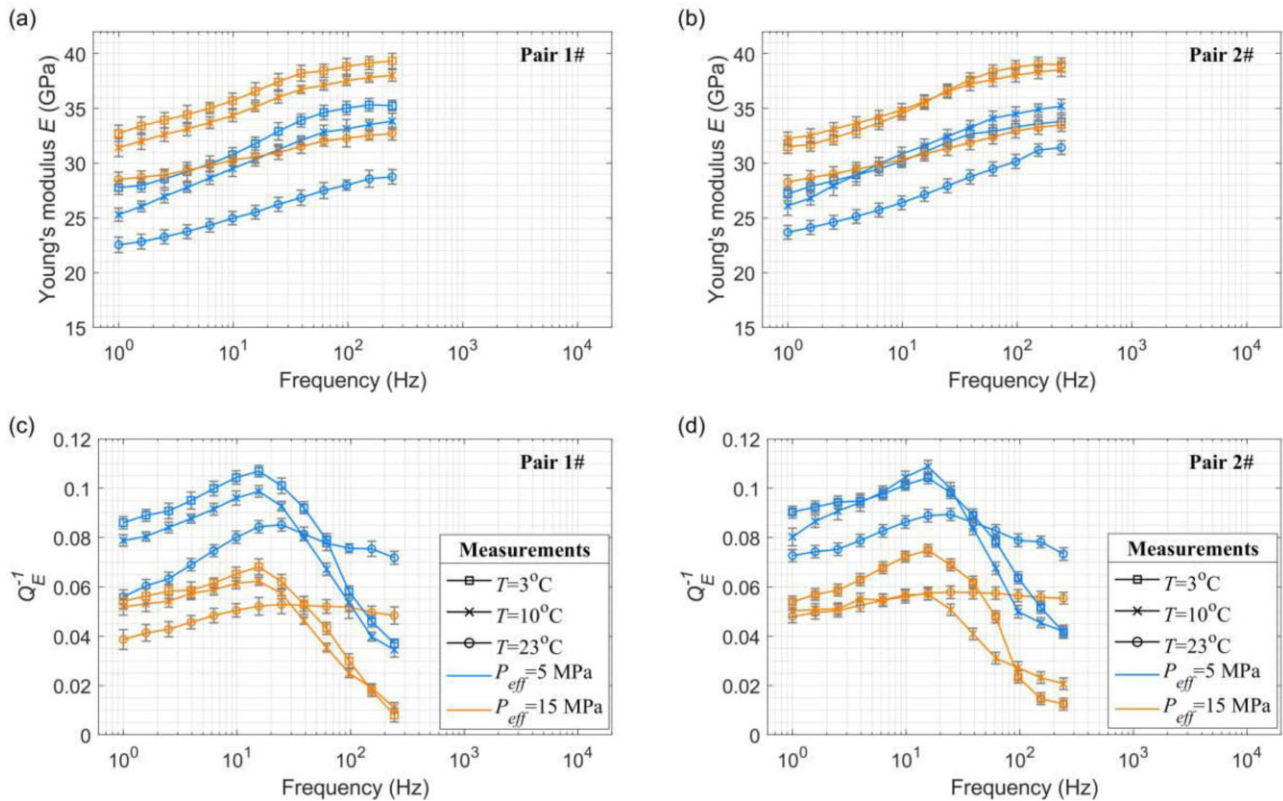
Figure 14. The measured frequency dependence of Young's modulus E and Young's attenuation Q_E^{-1} of a sandstone sample fully saturated with glycerine at $T = 23°\,C$ (open circle and line), $T = 10°\,C$ (cross and line), and $T = 3°\,C$ (open square and line) at two effective pressures $P_{eff} = [5,\ 15]\,MPa$. Note that the measured results from Pair 1# (a and c) and Pair 2# (b and d) represent the mean values of three experiments, with corresponding error bars reported.

This convergence indicates that at low frequencies, the fluid in the pores has enough time to equilibrate pressure, resulting in undrained conditions. In glycerine-saturated condition, there is significant dispersion around the characteristic frequency $2.5 \times 10^4\,Hz$, particularly at the low pressure $P_{eff} = 5\,MPa$. This dispersion is more pronounced compared to the brine-saturated condition, which shows dispersion around $150\,Hz$ that agrees with the predicted characteristic frequency f_{C2}^*. These observations are consistent with the drained/undrained transition frequencies, where the fluid cannot equilibrate pressure quickly enough at higher frequencies. As the apparent frequency f^a increases, the elastic moduli in glycerine-saturated condition increase towards values higher than the undrained predictions. This stiffening effect at higher frequencies is indicative of the squirt flow mechanism, where the restricted movement of fluid in compliant pores leads to an apparent increase in stiffness. This effect is more pronounced in glycerine-saturated sandstone due to glycerine's higher viscosity compared to brine.

The SFTPS model predicts bell-shaped attenuation curves that show a reasonably good fit with the measured results for brine- and glycerine-saturated conditions. These attenuation curves indicate the presence of two distinct squirt flow mechanisms: (1) between stiff and compliant pores, and (2) between intermediate and equant pores. The SFTPS model successfully predicts the amplitude of the attenuation peaks observed in the experimental data, however, it

does not accurately predict the frequency range of the second attenuation peak, particularly at higher pressure ($P_{eff} = 15\,MPa$). This discrepancy suggests that the pore microstructural parameters used in squirt flow calculations may not be accurately estimated from the rock's microscopic data obtained via SEM using the present parameter fitting method. The pressure effects on the dry moduli are complex, influenced by the rock's heterogeneous microstructures and varied pore types. These effects are not solely governed by the closure of microcracks but also by the interaction between different pore types and the overall structural heterogeneity (see Figs 1b to f). Additionally, the frequency bands of the measured attenuation Q_E^{-1} are significantly influenced by the position of local strain measurements. These measurements are averaged over paired results and may capture different fluid-flow regions at various scales. This variability can obscure the true attenuation characteristics, especially when ruling out other effects such as scattering, inertial influences, or patchy saturation (e.g. Borgomano *et al.* 2019). While it is impractical to completely preclude fluid flow due to mesoscopic heterogeneities at the sample scale, the contrasting compressibility of fluid-saturated regions does not seem to create significant attenuation amplitudes compared to those due to squirt flow associated with microscopic compressibility heterogeneities. Thus, at a given effective pressure, it is possible to identify distinct frequency ranges corresponding to drained, undrained and unrelaxed regimes. Furthermore, the presence of a second attenuation peak in
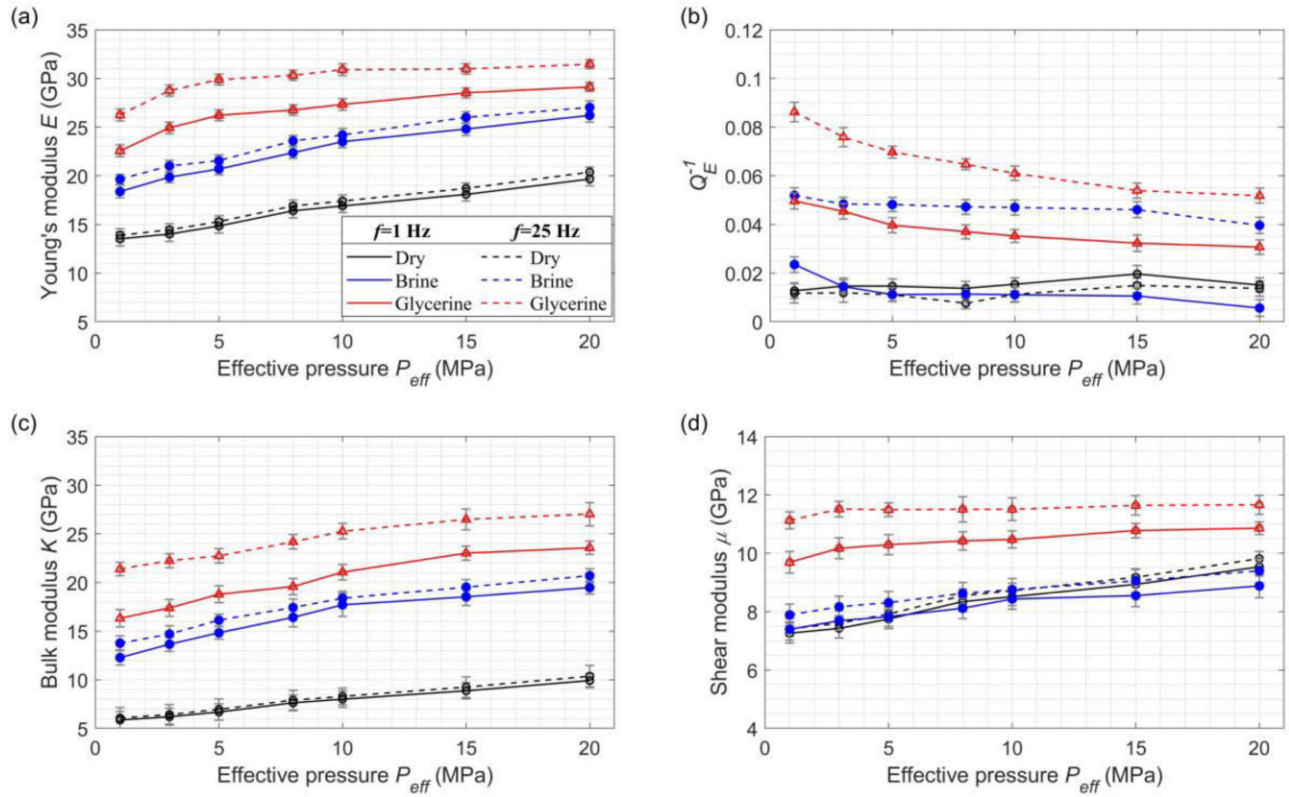
Figure 15. Laboratory measurements were conducted at frequencies of $f = [1, 25]$ Hz to observe the variations in Young's modulus E, Young's attenuation Q_E^{-1}, bulk modulus K and shear modulus μ with effective pressure P_{eff} for the tight sandstone saturated with nitrogen gas, brine and glycerine at $T = 23°$ C. At these frequencies, the elastic measurements are significantly affected by the pore infills.

glycerine-saturated results is consistent with the estimated characteristic frequency f_{C2}^*, supporting the presupposition that the squirt flow effects are related to the microheterogeneity of the rock's solid frame and pore fluids.

4.3 Fluid viscosity effects on pressure sensitivity of seismic attenuation and dispersion

The role of fluid viscosity on the frequency-dependent variations of Young's modulus E and attenuation Q_E^{-1} in microstructurally complex sandstone TS4 is intricately tied to temperature changes, which affect the viscosity of the saturating fluid. This relationship is specifically examined in the context of glycerine saturation at different temperatures and varying effective pressures ($P_{eff} = [5, 15]$ MPa), as illustrated in Fig. 14. The characteristic frequency of the squirt flow mechanism is inversely proportional to the viscosity of the saturating fluid. As temperature increases from 3 to 23°C, the viscosity of glycerine decreases, leading to a reduction in the visible attenuation peaks for both pairs of strain measurements (Figs 14c and d). The attenuation peaks correspond to a broader frequency band at higher temperatures because the reduced viscosity allows the fluid to flow more easily between pores. Moreover, this broadening of the frequency band and the drop in attenuation peak amplitude are likely due to the heterogeneous distributions of aspect ratios of the compliant and intermediate porosity, which strongly amplify the impact of fluid viscosity variations on the squirt flow mechanism. At seismic frequencies, the measured Young's modulus E from the two pairs of strain measurements (Pair 1# and Pair 2#) shows significant differences. This variation is likely related to the potential squirt flow

process, which is highly sensitive to minor variations in the rock's microstructures.

The experimental measurements of low-frequency elastic moduli and attenuation for sandstone TS4 under different saturating conditions (N_2-, brine- and glycerine-saturated) at 23°C, as depicted in Fig. 15, offer valuable insights into the frequency-dependent behaviour of the rock sample. The elastic moduli and attenuation vary significantly with effective pressure, highlighting the influence of the type of saturating fluid and the spatial distribution and scale of the heterogeneities within the rock matrix. At low frequencies, fluid pressure diffusion equilibrates throughout all the pores. This equilibration leads to a more homogeneous response at the representative elementary volume scale, resulting in elastic properties that are more consistent and isotropic across the rock sample. At higher frequencies, microscale wave-induced pressure gradients arise from fluid flow between pore types with contrasting compressibility. These gradients lead to deviations from the isobaric state, causing significant variations in elastic moduli and attenuation. The measured results indicate strong squirt flow dispersion affecting seismic frequencies, suggesting that squirt flow effects are significant and must be considered when interpreting seismic data. Squirt flow effects are not expected to be potentially independent of the measured location, provided that each saturated REV of the sample is considered the same. However, local strain measurement regions larger than an REV average area show variations, highlighting the importance of considering the local measurement area and inherent heterogeneities when interpreting elastic properties for accurate geophysical and reservoir applications.

5 CONCLUSIONS

Laboratory experiments on a microstructurally complex sandstone were conducted to delve into the effects of rock microheterogeneity on the dispersion and attenuation of elastic moduli. These experiments utilized a low-frequency forced axial oscillation method combined with the ultrasonic transmission method to monitor the evolution of dynamic elastic properties across different frequencies and effective pressures. The experiments were performed on a low-permeability sandstone specimen under three conditions: dry, brine-saturated, and glycerine-saturated. The elastic moduli exhibited no significant frequency dependence in the dry state, indicating a uniform response throughout the sample. Deviations from different measurement localizations of paired strain gauges were negligible, suggesting a consistent and homogeneous response in the absence of fluid. In contrast, under both brine- and glycerine-saturated conditions, noticeable dispersion and attenuation of elastic moduli were recorded, highlighting the role of fluid-induced heterogeneity-related dispersion mechanisms. Significant variations were observed across different local measurement areas, indicating that the presence of fluid amplifies the effects of rock microheterogeneities. At seismic frequencies, measurement differentiation tends to amplify, likely due to the squirt flow process influenced by microscopic compressibility heterogeneities within the rock matrix and saturating fluid. Despite common assumptions that the squirt flow effects on elastic properties are significant at higher frequencies and relatively independent of pore geometry intricacies, the experimental measurements show pronounced squirt flow dispersion within the seismic frequency band.

Under brine- and glycerine-saturated conditions, the measured elastic moduli of the sandstone significantly increased with both frequency and effective pressure across the testing frequency range. The strong dispersion of elastic moduli coincided with a peak in attenuation. Additionally, for measurements using saturating fluids of varying viscosities, the effects of dispersion and attenuation due to viscous fluid flows shifted across different temperature ranges. This emphasizes the importance of considering the impact of fluid viscosity on rock elastic properties, as changes in temperature can significantly alter fluid behaviour and, consequently, the rock's elastic response. Predicted results from the SFTPS model, which considers the rock's microstructure and pore types, closely align with laboratory measurements. This congruence suggests that the observed frequency-dependent attenuation and modulus dispersion in the seismic frequency range are related to the squirt flow process driven by microscopic compressibility heterogeneities at the measurement sites. Therefore, relying solely on low-frequency axial oscillation experiments and position-dependent strain measurements in microstructurally complex zones may lead to inaccuracies due to local variations in rock properties and fluid behaviour. These local variations can complicate interpretations in field applications, necessitating detailed microstructural models in geophysical studies, particularly in seismic hydrocarbon exploration and CO_2 geo-sequestration monitoring efforts.

ACKNOWLEDGMENTS

DATA AVAILABILITY

All experimental data and models presented in this study can be reproduced and are available at https://github.com/Mfw195/moduli-dispersion-attenuation.

REFERENCES

Adam, L., Batzle, M., Lewallen, K.T. & van Wijk, K., 2009. Seismic wave attenuation in carbonates, *J. geophys. Res.,* **114,** B06208.

Adelinet, M., Fortin, J., Guéguen, Y., Schubnel, A. & Geoffroy, L., 2010. Frequency and fluid effect on elastic properties of basalt: experimental investigations, *Geophys. Res. Lett.,* **37,** L02303, doi:10.1029/2009GL041660.

Alkhimenkov, Y., 2024. Simulating squirt flow in realistic rock models using graphical processing units (GPUs), *Geophys. J. Int.,* **238,** 272–289.

Alkhimenkov, Y. & Quintal, B., 2022. An accurate analytical model for squirt flow in anisotropic porous rocks –Part 2: complexgeometry, *Geophysics,* **87**(6), MR291–MR302.

Alkhimenkov, Y. & Quintal, B., 2024. A simple and accurate model for attenuation and dispersion caused by squirt flow in isotropic porous rocks, *Geophysics,* **89**(1), MR1–MR10.

Batzle, M.L., Han, D.H. & Hofmann, R., 2006. Fluid mobility and frequency-dependent seismic velocity—direct measurement, *Geophysics,* **71**(1), N1–N9.

Biot, M.A., 1962. Mechanics of deformation and acoustic propagation in porous media, *J. Appl. Phys.,* **33,** 1482–1498.

Borgomano, J.V.M., Pimienta, L., Fortin, J. & Guéguen, Y., 2017. Dispersion and attenuation measurements of the elastic moduli of a dual-porosity limestone, *J. Geophys. Res.: Solid Earth,* **122,** 2690–2711.

Borgomano, J.V.M., Pimienta, L., Fortin, J. & Gueguen, Y., 2019. Seismic dispersion and attenuation in fluid-saturated carbonate rocks: effects of microstructure and pressure, *J. Geophys. Res.: Solid Earth,* **124,** 2019JB018434.

Carcione, J. & Gurevich, B., 2011. Differential form and numerical implementation of Biot's poroelasticity equation with squirt dissipation, *Geophysics,* **76**(6), N55–N64.

Chapman, M., 2003. Frequency-dependent anisotropy due to mesoscale fractures in the presence of equant porosity, *Geophys. Prospect.,* **51,** 369–379.

Chapman, S., Borgomano, J., Yin, H.J., Fortin, J. & Quintal, B., 2019. Forced oscillation measurements of seismic wave attenuation and stiffness moduli dispersion in glycerine-saturated Berea sandstone, *Geophys. Prospect.,* **67,** 956–968.

Chapman, S., Quintal, B., Tisato, N. & Holliger, K., 2017. Frequency scaling of seismic attenuation in rocks saturated with two fluid phases, *Geophys. J. Int.,* **208,** 221–225.

Chapman, S., Tisato, N., Quintal, B. & Holliger, K., 2016. Seismic attenuation in partially saturated Berea sandstone submitted to a range of confining pressure, *J. Geophys. Res.: Solid Earth,* **121,** 2015JB012575.

Christensen, R.M., 1982. *Theory of Viscoelasticity: An Introduction.* Academic Press, New York.

Cole, K.S. & Cole, R.H., 1941. Dispersion and absorption in dieletrics I. Alternating current characteristics, *J. Chem. Phys.,* **9,** 341–351.

Cooper, R.F., 2002. Seismic wave attenuation: energy dissipation in viscoelastic crystalline solids, *Rev. Mineral. Geochem.,* **51**(1), 253–290.

David, E.C., Fortin, J., Schubnel, A., Guéguen, Y. & Zimmerman, W., 2013. Laboratory measurements of low- and high-frequency elastic moduli in Fontainebleau sandstone, *Geophysics,* **71**(5), N1–N9.

David, E.C. & Zimmerman, R.W., 2012. Pore structure model for elastic wave velocities in fluid-saturated sandstones, *J. geophys. Res.,* **117,** B07210.

Deng, W.B. & Morozov, I.B., 2016. Solid viscosity of fluid-saturated porous rock with squirt flows at seismic frequencies, *Geophysics,* **81**(4), D395–D404.

de Paula, O.B., Pervukhina, M., Makarynska, D. & Gurevich, B., 2012. Modeling squirt dispersion and attenuation in fluid-saturated rocks using pressure dependency of dry ultrasonic velocities, *Geophysics,* **77**(3), WA157–WA168.

Duan, C.S., Deng, J.X., Li, Y., Lu, Y.J., Tang, Z.Y. & Wang, X.B., 2018. Effect of pore structure on the dispersion and attenuation of fluid-saturated tight sandstone, *J. Geophys. Eng.,* **71,** N1–N9.

Dvorkin, J., Mavko, G. & Nur, A., 1995. Squirt flow in fully saturated rocks, *Geophysics,* **60,** 97–107.

Gassmann, F., 1951. Elasticwaves through a packing of spheres, *Geophysics,* **16,** 673–685.

Glubokovskikh, S., Gurevich, B. & Saxena, N., 2016. A dual-porosity scheme for fluid/solid substitution, *Geophys. Prospect.,* **64**(4), 1112–1121.

Gurevich, B. & Carcione, J.M., 2022. *Attenuation and Dispersion of Elastic Waves in Porous Rocks: Mechanisms and Models.* Society of Exploration Geophysicists.

Gurevich, B., Makarynska, D., de Paula, O.B. & Pervukhina, M., 2010. A simple model for squirt-flow dispersion and attenuation in fluid-saturated granular rocks, *Geophysics,* **75**(6), N109–N120.

Han, T.C., Liu, B.K. & Sun, J.M., 2018. Validating the theoretical model for squirt-flow attenuation in fluid saturated porous rocks based on the dual porosity concept, *Geophys. J. Int.,* **214,** 1800–1807.

He, Y.-X. *et al.*, 2023. Experimental mechanism of elastic parameters in saturated carbonate at seismic frequencies: role of pressure and pore fluid, *Chin. J. Geophys.,* **66**(12), 5141–5156.

He, Y.-X., Wang, S.X., Tang, G.Y., Dong, C.H., Sun, C., Yuan, S.Y. & Shi, P.D., 2024a. Experimental investigation of pore-filling substitution effect on frequency-dependent elastic moduli of Berea sandstone, *Geophys. J. Int.,* **238**(2), 902–921.

He, Y.-X. *et al.*, 2024b. A seismic elastic moduli module for the measurements of low-frequency wave dispersion and attenuation of fluid-saturated rocks under different pressures, *Petrol. Sci.,* **21,** 162–181.

He, Y.-X., Wang, S.X., Xi, B., Tang, G.Y., Yin, H.J., Zhao, L.M., Sun, C. & Ma, X.Y., 2022. Role of pressure and pore microstructure on seismic attenuation and dispersion of fluid-saturated rocks: laboratory experiments and theoretical modelling, *Geophys. J. Int.,* **231**(3), 1917–1937.

Huang, Q., Han, D.H. & Li, H., 2015. Laboratory measurements of dispersion and attenuation in the seismic frequency. *SEG Technical Program Expanded Abstracts, SEG,* 3090–3094.

Krief, M., Garat, J., Stellingwerff, J. & Ventre, J., 1990. A petrophysical interpretation using the velocities of P and S waves (full-waveform sonic), *Log Analyst,* **31,** 355–369.

Landau, L.D. & Lifshitz, E., 1969. *Statistical Physics: Pt. 1. Course of Theoretical Physics,* Pergamon International Library of Science.

Li, H., Wang, D.X., Gao, J.H., Zhang, M.B., Wang, Y.R., Zhao, L.X. & Yang, Z.F. 2019. Role of saturation on elastic dispersion and attenuation of tight rocks: an experimental study, *J. Geophys. Res.,* **125,** e2019JB018513, doi: 10.1029/2019JB018513.

Lienert, B.R. & Manghnai, M.H., 1990. The relationship between $1/Q_E$ and dispersion in extensional modulus, *E*, *Geophys. Res. Lett.,* **17**(6), 677–680.

Lissa, L., Barbosa, N.D., Caspari, E., Alkhimenkov, Y. & Quintal, B. 2020. Squirt flow in cracks with rough walls, *J. Geophys. Res.: Solid Earth,* **125,** e2019JB019235, doi:10.1029/2019JB019235.

Lozovyi, S. & Bauer, A., 2019. From static to dynamic stiffness of shales: frequency and stress dependence, *Rock Mech. Rock Eng.,* **52,** 5085–5098.

Mavko, G., 2013. Relaxation shift in rocks containing viscoelastic pore fluids, *Geophysics,* **78**(3), M19–M28.

Mavko, G. & Jizba, D., 1991. Estimating grain-scale fluid effects on velocity dispersion in rocks, *Geophysics,* **56**(12), 1940–1949.

Mavko, G., Mukerji, T. & Dvorkin, J., 2009. *The Rock Physics Handbook: Tools for Seismic Analysis of Porous media.* Cambridge University Press, Cambridge.

Mikhaltsevitch, V., Lebedev, M. & Gurevich, B., 2014. A laboratory study of low-frequency wave dispersion and attenuation in water-saturated sandstones, *The Leading Edge,* **33**(6), 616–618.

Mikhaltsevitch, V., Lebedev, M. & Gurevich, B., 2016a. Laboratory measurements of the effect of fluid saturation on elastic properties of carbonates at seismic frequencies: effect of fluid saturation on carbonates, *Geophys. Prospect.,* **64**(4), 799–809.

Mikhaltsevitch, V., Lebedev, M. & Gurevich, B., 2016b. Validation of the laboratory measurements at seismic frequencies using the Kramers-Kronig relationship, *Geophys. Res. Lett.,* **43,** 4986–4991.

Mikhaltsevitch, V., Lebedev, M., Pervukina, M. & Gurevich, B., 2021. Seismic dispersion and attenuation in Mancos shale—laboratory measurement, *Geophys. Prospect.,* **69,** 568–585.

Müller, T.M., Gurevich, B. & Lebedev, M., 2010. Seismic wave attenuation and dispersion resulting from wave-induced flow in porous rocks—a review, *Geophysics,* **75**(5), A147–A164.

O'Connell, R.J. & Budiansky, B., 1977. Viscoelastic properties of fluid-saturated cracked solids, *J. geophys. Res.,* **82,** 5719–5740.

O'Donnel, M., Jaynes, E.T. & Miller, J.G., 1981. Kramers-Kronig relationship between ultrasonic attenuation and phase velocity, *Acoust. Soc. Am.,* **69**(3), 696–701.

Piane, L., Sarout, J., Madonna, C., Saenger, E.H., Dewurst, D.N. & Raven, M., 2014. Frequency-dependent seismic attenuation in shale: experimental results and theoretical analysis, *Geophys. J. Int.,* **198**(1), 504–515.

Pimienta, L., Borgomano, J., Fortin, J. & Guéguen, Y., 2017. Elastic dispersion and attenuation in fully saturated sandstones: role of mineral content, porosity, and pressures, *J. Geophys. Res.: Solid Earth,* **122,** 9950–9965.

Pimienta, L., Fortin, J. & Guéguen, Y., 2015. Experimental study of Young's modulus dispersion and attenuation in fully saturated, *Geophysics,* **80**(5), L57–L72.

Pride, S.R., Berryman, J.G. & Harris, J., 2004. Seismic attenuation due to wave-induced flow, *J. geophys. Res.,* **109,** B01201.

Quintal, B., Rubino, J.G., Caspari, E. & Hilliger, K., 2016. A simple hydromechanical approach for simulating squirt-type flow, *Geophysics,* **81**(4), D335–D344.

Rorheim, S., Bauer, A. & Holt, R.M., 2022. On the low-frequency elastic response of Pierre Shale during temperature cycles, *Geophys. J. Int.,* **228,** 1260–1280.

Rubino, J.G. & Holliger, K., 2013. Research note: seismic attenuation due to wave-induced fluid flow at microscopic and mesoscopic scales, *Geophys. Prospect.,* **61,** 882–889.

Sahoo, S.K., North, L.J., Marín-Moreno, H., Minshull, T.A. & Best, A.I., 2019. Laboratory observation of frequency-dependent ultrasonic P-wave velocity and attenuation during methane hydrate formation in Berea sandstone, *Geophys. J. Int.,* **219**(1), 713–723.

Sarout, J., 2012. Impact of pore space topology on permeability, cut-off frequencies and validity of wave propagation theories: pore space topology and wave propagation, *Geophys. J. Int.,* **189**(1), 481–492.

Shapiro, S.A., 2003. Elastic piezosensitivity of porous and fractured rocks, *Geophysics,* **68,** 428–486.

Sheng, Z.Z. & Jian, J.W., 1998. A experimental formula of glycerine viscosity coefficient's variation with temperature, *J. Xinjiang Petrol. Inst.,* **1**(10), 68–70.

Spencer, J.W., 1981. Stress relaxations at low frequencies in fluid saturated rocks: attenuation and modulus dispersion, *J. Geophys. Res.: Solid Earth,* **42**(C5), 1175–1180.

Spencer, J.W., 2013. Viscoelasticity of Ells River bitumen sand and 4D monitoring of thermal enhanced oil recovery processes, *Geophysics,* **78**(6), D419–D428.

Spencer, J.W. & Shine, J., 2016. Seismic wave attenuation and modulus dispersion in sandstones, *Geophysics,* **81**(3), D211–D231.

Subramaniyan, S., Quintal, B., Madonna, C. & Saenger, E.H., 2015. Laboratory-based seismic attenuation in Fontainebleau sandstone: evidence of squirt flow, *J. Geophys. Res.: Solid Earth,* **120,** 7526–7535.

Sun, C., Fortin, J., Borgomano, J., Wang, S.X., Tang, G.Y., Bultreys, T. & Cnudder, V., 2022. Influence of fluid distribution on seismic dispersion and attenuation in partially saturated limestone, *J. Geophys. Res.: Solid Earth,* **127,** e2021JB023867, doi:10.1029/2021JB023867.

Sun, C., Tang, G.Y., Fortin, J., Borgomano, J. & Wang, S.X., 2020. Dispersion and attenuation of elastic wave velocities: impact of microstructure heterogeneities and local measurements, *J. Geophys. Res.: Solid Earth,* **125,** e2020JB020132, doi:10.1029/2020JB020132.

Sun, Y.Y. & Gurevich, B., 2020. Modeling the effect of pressure on the moduli dispersion in fluid-saturated rocks, *J. Geophys. Res.: Solid Earth,* **125,** e2019JB019297.

Szewczyk, D., Bauer, A. & Holt, R.M., 2018. Stress-dependent elastic properties of shale—laboratory experiment at seismic and ultrasonic frequencies, *Geophys. J. Int.,* **212,** 189–210.

Tisato, N. & Quintal, B., 2013. Measurements of seismic attenuation and transient fluid pressure in partially saturated Berea sandstone: evidence of fluid flow on the mesoscopic scale, *Geophys. J. Int.,* **195,** 342–351.

Tisato, N., Quintal, B., Chapman, S., Podladchikov, Y. & Burg, J.-P., 2015. Bubbles attenuate elastic waves at seismic frequencies: first experimental evidence, *Geophys. Res. Lett.,* **42,** 3880–3887.

Wei, Q.Q., Wang, Y., Han, D.H. & Huang, Q. 2021. Combined effects of permeability and fluid saturation on seismic wave dispersion and attenuation in partially-saturated sandstone, *Adv. Geo-Energy Res.,* **5**(2), 181–190.

Yin, H.J., Zhao, J.G., Tang, G.Y., Zhao, L.M., Ma, X.Y. & Wang, S.X., 2017. Pressure and fluid effects on frequency-dependency-dependent elastic moduli in fully saturated tight sandstone, *J. Geophys. Res.: Solid Earth,* **122,** 2017JB014244.

Zhang, M.F., He, Y.-X., Wang, S.X., Tang, G.Y. & Sun, C., 2023. A benchmark study for quasi-static numerical upscaling of seismic wave attenuation and dispersion in fractured poroelastic rocks, *Comput. Geosci.,* **180,** 105 459, doi:10.1016/j.cageo.2023.105459.

Zhao, L.M., Tang, G.Y., Sun, C., Zhao, J.G. & Wang, S.X., 2021. Dual attenuation peaks revealing mesoscopic and microscopic fluid flow in partially oil-saturated Fontainebleau sandstones, *Geophys. J. Int.,* **224,** 1670–1683.

Zhao, L.X., Yuan, H.M., Yang, J.K., Han, D.H., Geng, J.H., Zhou, R., Li, H. & Yao, Q.L., 2017. Mobility effect on poroelastic seismic signatures in partially saturated rocks with applications in time-lapse monitoring of a heavy oil reservoir, *J. Geophys. Res.: Solid Earth,* **122,** 8872–8891.